Chapter 6

Muon spectrometer

6.1 Overview

The muon spectrometer forms the outer part of the ATLAS detector and is designed to detect charged particles exiting the barrel and end-cap calorimeters and to measure their momentum in the pseudorapidity range $|\eta| < 2.7$. It is also designed to trigger on these particles in the region $|\eta| < 2.4$. The driving performance goal is a stand-alone transverse momentum resolution of approximately 10% for 1 TeV tracks, which translates into a sagitta along the z (beam) axis of about 500 μm, to be measured with a resolution of ≤ 50 μm. Muon momenta down to a few GeV (~ 3 GeV, due to energy loss in the calorimeters) may be measured by the spectrometer alone. Even at the high end of the accessible range (~ 3 TeV), the stand-alone measurements still provide adequate momentum resolution and excellent charge identification. A general overview of the acceptance coverage and the chamber types for precision measurements and triggering is given in section 1.4.

Precision-tracking chambers in the barrel region are located between and on the eight coils of the superconducting barrel toroid magnet, while the end-cap chambers are in front and behind the two end-cap toroid magnets. The ϕ symmetry of the toroids is reflected in the symmetric structure of the muon chamber system, consisting of eight octants. Each octant is subdivided in the azimuthal direction in two sectors with slightly different lateral extensions, a large and a small sector, leading to a region of overlap in ϕ. This overlap of the chamber boundaries minimises gaps in detector coverage and also allows for the relative alignment of adjacent sectors using tracks recorded by both a large and a small chamber (see section 10.3.2).

The chambers in the barrel are arranged in three concentric cylindrical shells around the beam axis at radii of approximately 5 m, 7.5 m, and 10 m. In the two end-cap regions, muon chambers form large wheels, perpendicular to the z-axis and located at distances of $|z| \approx 7.4$ m, 10.8 m, 14 m, and 21.5 m from the interaction point. Figures 6.1 and 6.2 give cross-sections in the planes transverse to, and containing, the beam axis, while figure 6.3 [160] shows the overall layout of the muon system. In the centre of the detector ($|\eta| \approx 0$), a gap in chamber coverage has been left open to allow for services to the solenoid magnet, the calorimeters and the inner detector. The size of the gap varies from sector to sector depending on the service necessities, the biggest gaps of 1-2 m being located in the large sectors. The angular range, seen from the interaction point,

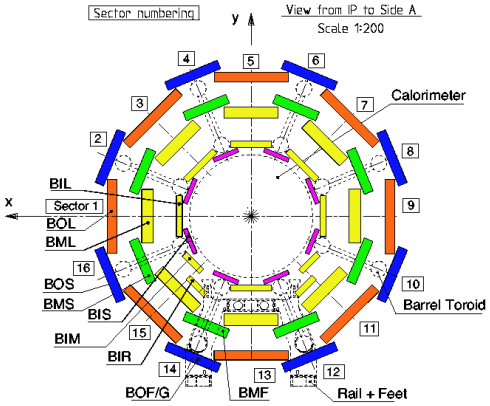

Figure 6.1: Cross-section of the barrel muon system perpendicular to the beam axis (non-bending plane), showing three concentric cylindrical layers of eight large and eight small chambers. The outer diameter is about 20 m.

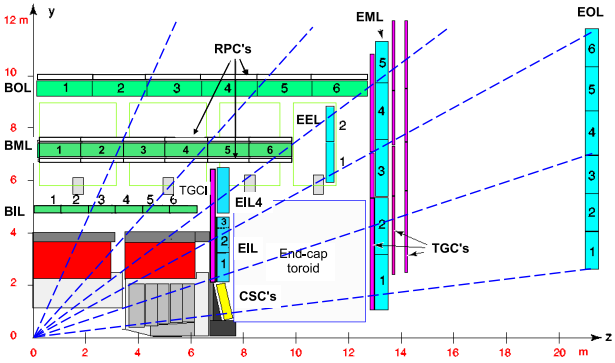

Figure 6.2: Cross-section of the muon system in a plane containing the beam axis (bending plane). Infinite-momentum muons would propagate along straight trajectories which are illustrated by the dashed lines and typically traverse three muon stations.

where a high momentum (straight) track is not recorded in all three muon layers due to the gaps is about $\pm 4.8^\circ$ ($|\eta| \leq 0.08$) in the large and $\pm\ 2.3^\circ$ ($|\eta| \leq 0.04$) in the small sectors. Additional gaps in the acceptance occur in sectors 12 and 14 due to the detector support structure (feet). The consequences of the acceptance gaps on tracking efficiency and momentum resolution are shown in figures 10.37 and 10.34, respectively. A detailed discussion is given in section 10.3.4.

The precision momentum measurement is performed by the Monitored Drift Tube chambers (MDT's), which combine high measurement accuracy, predictability of mechanical deformations and simplicity of construction (see section 6.3). They cover the pseudorapidity range $|\eta| < 2.7$ (except in the innermost end-cap layer where their coverage is limited to $|\eta| < 2.0$). These chambers consist of three to eight layers of drift tubes, operated at an absolute pressure of 3 bar, which achieve an average resolution of 80 μm per tube, or about 35 μm per chamber. An illustration of a 4 GeV and a 20 GeV muon track traversing the barrel region of the muon spectrometer is shown in figure 6.4. An overview of the performance of the muon system is given in [161].

In the forward region ($2 < |\eta| < 2.7$), Cathode-Strip Chambers (CSC) are used in the innermost tracking layer due to their higher rate capability and time resolution (see section 6.4). The CSC's are multiwire proportional chambers with cathode planes segmented into strips in orthogonal directions. This allows both coordinates to be measured from the induced-charge distribution. The resolution of a chamber is 40 μm in the bending plane and about 5 mm in the transverse plane. The difference in resolution between the bending and non-bending planes is due to the different readout pitch, and to the fact that the azimuthal readout runs parallel to the anode wires. An illustration of a track passing through the forward region with $|\eta| > 2$ is shown in figure 6.5.

To achieve the sagitta resolution quoted above, the locations of MDT wires and CSC strips along a muon trajectory must be known to better than 30 μm. To this effect, a high-precision optical alignment system, described in section 6.5, monitors the positions and internal deformations of the MDT chambers; it is complemented by track-based alignment algorithms briefly discussed in section 10.3.2.

2008 JINST 3 S08003

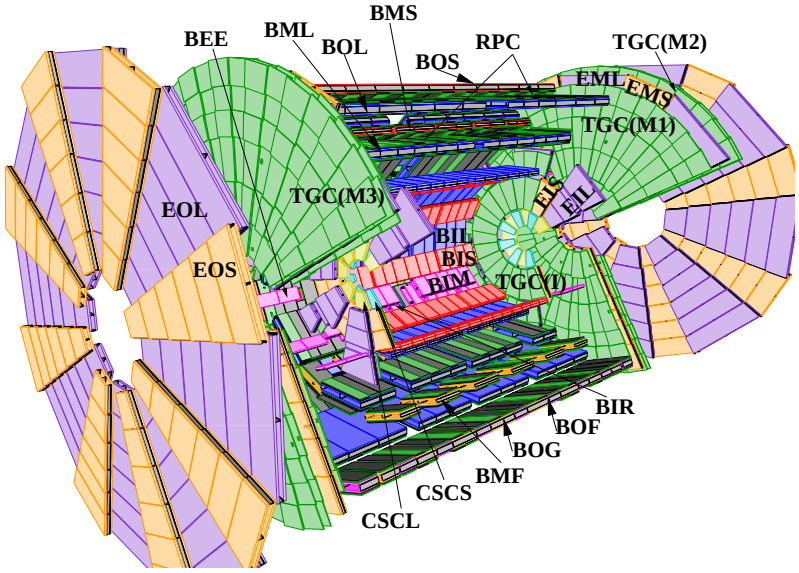

Figure 6.3: Initial configuration of the muon spectrometer with its four chamber sub-systems: the precision-measurement tracking chambers (MDT's and CSC's) and the trigger chambers (RPC's and TGC's). In the end-cap, the first TGC layer (I) is located in front of the innermost tracking layer; the next three layers stand in front (M1) and behind (M2 and M3) the second MDT wheel. The first letter (B and E) of the MDT naming scheme refers to barrel and end-cap chambers, respectively. The second and third letters refer to layer (inner, middle, and outer) and sector (large and small) types, respectively (see section 6.3.1).

An essential design criterion of the muon system was the capability to trigger on muon tracks. The precision-tracking chambers have therefore been complemented by a system of fast trigger chambers capable of delivering track information within a few tens of nanoseconds after the passage of the particle. In the barrel region ($|\eta| < 1.05$), Resistive Plate Chambers (RPC) were selected for this purpose (section 6.7), while in the end-cap ($1.05 < |\eta| < 2.4$) Thin Gap Chambers (TGC) were chosen (section 6.8). Table 6.1 gives the intrinsic time resolution of the detectors, to which contributions from signal propagation and electronics have to be added. The design goal was to keep these contributions low enough for reliable beam-crossing identification with $\geq 99\%$ probability. Both chamber types deliver signals with a spread of 15–25 ns, thus providing the ability to tag the beam-crossing. The trigger chambers measure both coordinates of the track, one in the bending (η) plane and one in the non-bending (ϕ) plane.

The purpose of the precision-tracking chambers is to determine the coordinate of the track in the bending plane. After matching of the MDT and trigger chamber hits in the bending plane, the trigger chamber's coordinate in the non-bending plane is adopted as the second coordinate of the MDT measurement. This method assumes that in any MDT/trigger chamber pair a maximum of one track per event be present, since with two or more tracks the η and ϕ hits cannot be combined in an unambiguous way. Simulations have shown that the probability of a track in the

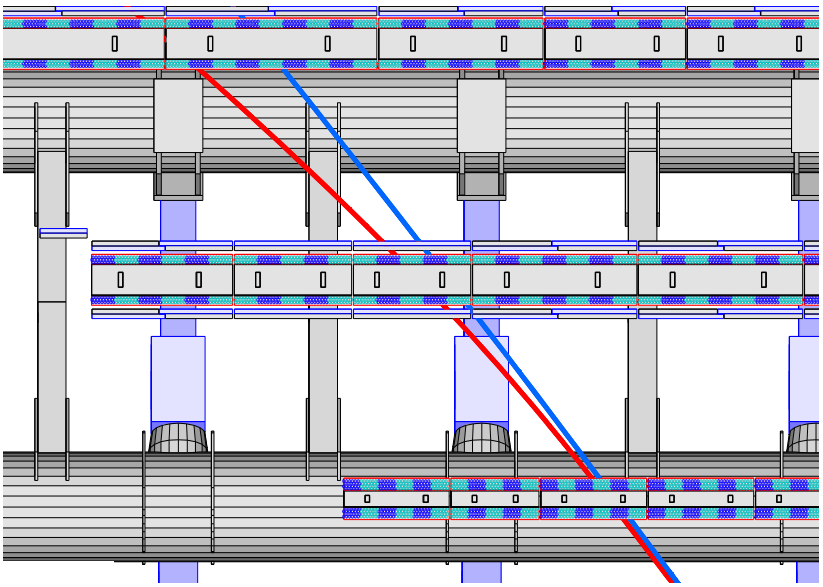

Figure 6.4: Trajectories of muons with momenta of 4 GeV and 20 GeV in the bending plane of the barrel muon spectrometer. In general, the tracks cross 2×4 inner, 2×3 middle, and 2×3 outer layers of MDT tubes. The cyan and dark blue areas in each MDT layer illustrate the granularity of the mezzanine cards (section 6.3.3).

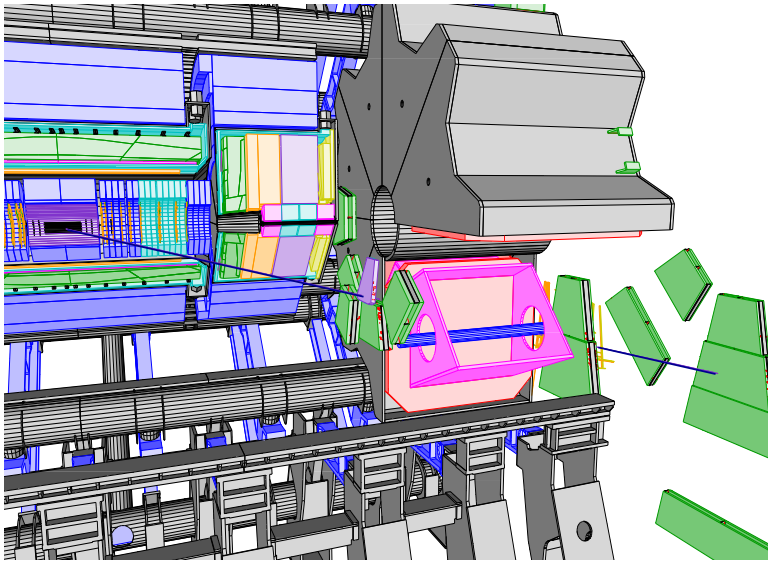

Figure 6.5: Structure of the barrel and end-cap regions with a track at large η, passing through a CSC in the inner wheel and through MDT's in the middle and outer wheels. For $|\eta| > 2.0$, the 2×4 hits in the inner MDT, as explained in figure 6.4, are replaced by four CSC hits.

Table 6.1: Parameters of the four sub-systems of the muon detector. The quoted spatial resolution (columns 3, 4) does not include chamber-alignment uncertainties. Column 5 lists the intrinsic time resolution of each chamber type, to which contributions from signal-propagation and electronics contributions need to be added. Numbers in brackets refer to the complete detector configuration as planned for 2009.

		Chamber resolution (RMS) in			Measurements/track		Number of	
Type	**Function**	z/R	ϕ	time	barrel	end-cap	chambers	channels
MDT	tracking	35 μm (z)	—	—	20	20	1088 (1150)	339k (354k)
CSC	tracking	40 μm (R)	5 mm	7 ns	—	4	32	30.7k
RPC	trigger	10 mm (z)	10 mm	1.5 ns	6	—	544 (606)	359k (373k)
TGC	trigger	2–6 mm (R)	3–7 mm	4 ns	—	9	3588	318k

muon spectrometer with $p_T > 6\,\text{GeV}$ is about 6×10^{-3} per beam-crossing, corresponding to about 1.5×10^{-5} per chamber. Assuming uncorrelated tracks, this leads to a negligible probability to find more than one track in any MDT/trigger chamber pair. When *correlated* close-by muon tracks do occur, caused for example by two-body-decays of low-mass particles, the ambiguity in η and ϕ-assignment will be resolved by matching the muon track candidates with tracks from the inner detector.

The muon system was designed to tolerate the radiation levels in the experimental hall, which may induce ageing effects in the detectors and damage the electronics. All components were therefore tested to withstand at least five times the radiation levels predicted by the simulation studies (see section 3.3.2).

Due to budget constraints, parts of the muon spectrometer have been staged. This includes the readout electronics of certain RPC trigger chambers in the feet region, which will only be installed in 2009. It also affects the MDT chambers in the transition region between barrel and end-cap (EE chambers), the construction of which has been completed and their installation expected in 2009. In table 6.1, the numbers in parentheses correspond to the completed detector.

6.2 Precision-tracking chambers

The overall layout of the MDT's is projective: the layer dimensions and the chamber sizes increase in proportion of their distance from the interaction point. The MDT chambers cover the region $|\eta| < 2.7$, except for the innermost layer where they are replaced by CSC's for $2 < |\eta| < 2.7$. In the initial configuration of the spectrometer at the start-up of the LHC, there are 1088 MDT chambers with 18 main types in the detector for a total area of $5500\,\text{m}^2$. Besides the main type of chambers, a considerable number of chambers with special shapes have been built to minimise acceptance losses in the regions around the magnet coils and support structures, as illustrated by the many different MDT chamber names in figure 6.3.

The particle fluxes and muon-track density are highest in the forward direction ($2 < |\eta| < 2.7$). These issues, which directly impact the pattern recognition and the muon-reconstruction efficiency as well as the radiation ageing of the detectors, are particularly severe in the first forward

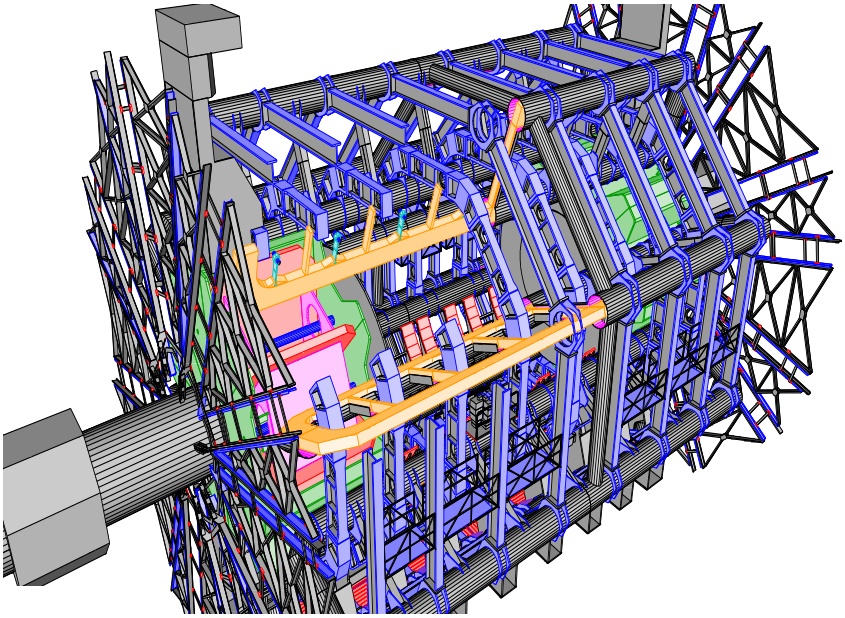

Figure 6.6: Overall three-dimensional view of the passive material in the muon system, which consists of such items as the barrel and end-cap toroid coils and vacuum vessels, as well as the support structures of the calorimeters, muon chambers, and toroid magnets.

muon-chamber layer, just downstream of the end-cap calorimeter. This layer is therefore equipped with CSC's, which measure both track coordinates simultaneously; multitrack ambiguities are resolved by correlating the magnitude of the charge collected on the two planes of orthogonal strips. Each track is measured in four consecutive CSC planes. The number of CSC measurements along a track is less than in the MDT's; however, the faster time response helps restore the tracking efficiency. The CSC's cover an area of about 65 m^2 in total.

The air-core magnet concept for the muon spectrometer minimises the amount of material traversed by the muons after exiting the calorimeters. However, the muons also encounter the muon chambers themselves and their supports, as well as other passive materials such as the toroid coils, vacuum vessels and magnet support structures (figure 6.6). In the barrel, chambers are mounted on aluminium structures supported by the coils of the toroid magnet. In the end-cap, special wheel-like aluminium support structures have been built to carry the MDT's, TGC's and their respective services. Figure 6.7 shows the material to be transversed by a muon in one octant in units of

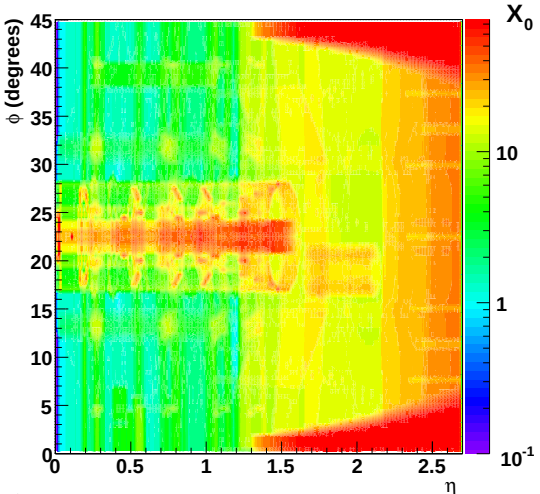

Figure 6.7: Amount of material in units of radiation lengths (X_0) traversed by muons after exiting the calorimeters, as a function of η and ϕ.

radiation lengths (X_0). A barrel-toroid coil is visible in this figure at $\phi = 22.5^\circ$ and two half-end-cap coils at $\phi = 0^\circ$ and 45°. The increase in radiative thickness above $\eta \sim 1.4$ is caused primarily by the heavy mechanical structure of the end-cap toroid. Over a large fraction of the acceptance in the barrel toroid, the cumulative amount of material traversed by a muon is about 1.3 X_0. As a consequence, multiple scattering effects dominate the momentum resolution between 30 GeV and 200 GeV.

6.3 Monitored drift tube chambers

6.3.1 Structure and function of the drift tube

The basic element of the monitored drift tube chambers is a pressurised drift tube with a diameter of 29.970 mm, operating with Ar/CO_2 gas (93/7) at 3 bar (see figure 6.8). The electrons resulting from ionisation are collected at the central tungsten-rhenium wire with a diameter of 50 μm, at a potential of 3080 V. The wire is held in position at the tube ends by a cylindrical end-plug (figure 6.9) which guarantees the concentricity of the wire with respect to the tube with an accuracy of $\sigma < 10$ μm. The central conductor holding the wire also serves for the gas transfer in and out of the tube. Signal transmission to the electronics and connection to the HV supply system are at opposite ends. The choice of the operating parameters of the drift tubes is discussed in [162–164].

Building the precision-tracking chambers out of individual tubes offers several advantages. The stiffness of the tube assembly allows to combine high mechanical precision with robustness of the chambers. A high level of operational reliability can be expected because the failure of a single tube does not affect the operation of most of the others. The tube concept lends itself to high-pressure operation, thereby reducing the deleterious effect of diffusion on the single-wire resolution. One more advantage is that the cylindrical geometry results in a radial electric field: the measurement accuracy, therefore, depends only weakly on the angle of incidence of the track onto the chamber plane, as the coordinate of the track is determined by the radius of the circle around the wire to which the track is tangential (see figure 6.8). This is important as the angle of incidence of infinite momentum tracks onto the chamber plane extends up to 45°. In a rectangular drift geometry, the field lines are such that the path length travelled by a electron resulting from ionisation would vary significantly depending on where along the muon track that electron is produced, thereby degrading the drift-time resolution.

A disadvantage of the radial drift geometry is the long pulse train caused by the track segments far from the tangential point, which may produce several threshold crossings (hits) per track. The maximum drift time from the wall to the wire is about 700 ns. A track passing close to the wire thus generates a pulse train with a duration of this order, while only the arrival time of the central track part, closest to the wire, is relevant for the track coordinate ($r_{\min}$ in figure 6.8). To prevent an inflation of the data volume by multiple track hits, an adjustable dead-time has been implemented in the front-end of the readout chain, see section 6.3.3.

The operating gas was selected because of the good ageing properties. Deposits on the wires have never been observed in clean samples of this gas mixture, the formation of polymers not being possible in the absence of hydrogen. A high degree of cleanliness is however required in all parts of the gas system as traces of hydrocarbons or silicon oil may lead to deposits on the wires and a

2008 JINST 3 S08003

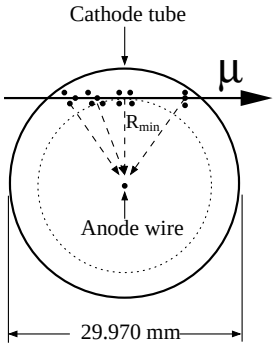

Figure 6.8: Cross-section of a MDT tube.

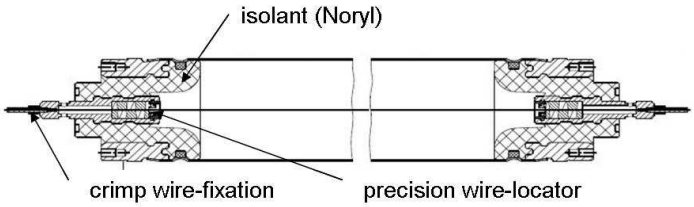

Figure 6.9: Longitudinal cut through a MDT tube.

reduction of the signal pulse height [165–168]. A disadvantage of this gas mixture is the non-linear space-drift time relation and the drift time of about 700 ns, which is about 50% longer than is typical for linear gases such as Ar/CH_4. The non-linearity of the Ar/CO_2 gas leads to a reduction of spatial resolution at high counting rates due to the distortion of the electric field created by the positive ions. At full LHC luminosity, counting rates of up to 30 kHz per tube will be expected due to the conversion of background photons and neutrons [34, 36, 169]. The corresponding degradation of the average resolution has been determined in tests at high gamma backgrounds and is expected to be 60-80 μm per tube at the expected background levels [166, 170–172]. Detailed results are given in section 6.3.4. An additional complication for tracking comes from the fact that the detailed shape of the space drift-time relation in $ArCO_2$ depends on environmental parameters like temperature and pressure as well as on the local magnetic field due to the Lorenz force. In order to maintain the high spatial resolution under varying environmental conditions, an online calibration system based on measured tracks is foreseen [173, 174].

A small water admixture to the gas of about 300 ppm is foreseen to improve HV stability. The effect of this admixture on the drift behaviour is expected to be negligible [175].

6.3.2 Mechanical structure

The main parameters of the MDT chambers are listed in table 6.2. The chambers are rectangular in the barrel and trapezoidal in the end-cap. Their shapes and dimensions were chosen to optimise solid angle coverage, while respecting the envelopes of the magnet coils, support structures and access ducts. The direction of the tubes in the barrel and end-caps is along ϕ, i.e. the centre points of the tubes are tangential to circles around the beam axis. While all tubes of a barrel chamber are of identical length (with the exception of some chambers with cut-outs), the tube lengths in the end-cap chambers vary along R in steps of 24 tubes. Detailed information on chamber dimensions and other parameters is available in [176]. The MDT chamber construction is described in [177].

The naming of chambers is based on their location in the barrel or end-cap (B,E), their assignment to inner, middle, or outer chamber layer (I, M, O) and their belonging to a large or a small sector (L,S). The sector number (1–16) and the sequence number of the chamber in a row of chambers in a sector are added to completely specify a MDT chamber. A BOS chamber, for example, is located in a small sector of the barrel, outer layer, while an EML lies in the large sec-

Table 6.2: Main MDT chamber parameters.

Parameter	Design value
Tube material	Al
Outer tube diameter	29.970 mm
Tube wall thickness	0.4 mm
Wire material	gold-plated W/Re (97/3)
Wire diameter	50 μm
Gas mixture	$Ar/CO_2/H_2O$ (93/7/$\leq$ 1000 ppm)
Gas pressure	3 bar (absolute)
Gas gain	2 x 10^4
Wire potential	3080 V
Maximum drift time	$\sim$ 700 ns
Average resolution per tube	$\sim$ 80 μm

tor of the middle layer of the end-cap. In sectors 12 and 14 (see figure 6.1) of the barrel, special chambers were designed to keep the acceptance losses due to the ATLAS support structure ("feet") to a minimum. Modified BOS chambers are therefore called BOF or BOG, and the modified BMS chambers BMF. The BEE (Barrel End-cap Extra) are special chambers located in the castellations of the end-cap toroid cryostats. Although labelled barrel chambers, the BEE are used in the measurement of tracks passing from the barrel to the end-cap. The BEE chambers consist of a single multi-layer of four tube layers.

As can be seen in figure 6.2, the outer part (in the radial direction) of the EI wheel does not project into the EO wheel. In order to allow for momentum measurement in this region, an intermediate ring of chambers, the EES and EEL (the "E" is derived from extra) chambers, have been introduced with an offset of about 3-3.6 m with respect to the corresponding EI wheel chambers.

All regular MDT chambers consist of two groups of tube layers, called multi-layers, separated by a mechanical spacer. In the innermost layer of the muon detector, each multi-layer consists of four tube layers to enhance the pattern-recognition performance; in the middle and outer layer of the muon detector, each multi-layer consists of three tube layers only. Figure 6.10 shows the structure of a barrel chamber with 2 $\times$ 3 tube layers. The height of the support beam between the multi-layers (spacer) depends on the chamber type, varying from 6.5 mm to 317 mm (tables 6.3 and 6.4). Detailed information about chamber dimensions and other parameters is available in [176].

During chamber construction, a high precision of tube placement and a high level of mechanical strength had to be achieved in order to maintain the inherent resolution of the drift tubes. The two multi-layers of a MDT chamber are mounted on a support frame of solid aluminium beams, providing mechanical rigidity to the structure. The lateral support beams (cross-plates), designated by RO for readout and HV for the high voltage supply side, are interconnected by two longitudinal beams. Three kinematic mounting points, not shown in figure 6.10, are attached to the frame for installation onto the rail system of ATLAS.

The frames also carry most of the interfaces to gas supplies, and to the electrical, monitoring and alignment services. The 3 (4) tube layers of a multi-layer are joined together with epoxy glue, layer by layer, after having been carefully aligned on a granite table. The reference surface for the

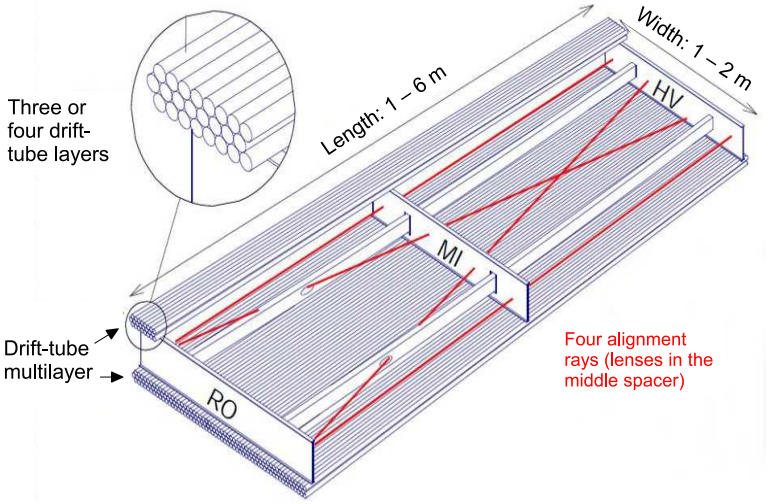

Figure 6.10: Mechanical structure of a MDT chamber. Three spacer bars connected by longitudinal beams form an aluminium space frame, carrying two multi-layers of three or four drift tube layers. Four optical alignment rays, two parallel and two diagonal, allow for monitoring of the internal geometry of the chamber. RO and HV designate the location of the readout electronics and high voltage supplies, respectively.

tubes is the precisely-milled end-plug, which also serves as reference for wire positioning. This method ensures a high precision of relative wire positioning at construction time.

The straightness of the tubes is required to be better than 100 μm. The relative positioning of wires reached during production, has been verified to be better than 20 μm. The gap between adjacent tubes filled by glue is 60 μm. A detailed account of MDT chamber construction and quality assurance is given in [178–183].

In spite of the solid construction of the MDT chambers, deformations are expected to occur in the various mounting positions in ATLAS and may change in time when thermal gradients are present. Therefore, an internal chamber alignment system was implemented, which continuously monitors potential deformations of the frame. The alignment system consists of a set of four optical alignment rays, two running parallel to the tube direction and two in the diagonal direction as shown in figure 6.10. The lenses for the light rays are housed in the middle, while LED's and CCD sensors are located in the outer spacers. This system can record deformations of a few μm and is designed to operate during production, installation, and operation of ATLAS. Details of the in-plane alignment system of the MDT chambers are given in section 6.5.

Due to gravitational forces, chambers are not perfectly straight but suffer a certain elastic deformation. The BOS chambers for example, with a tube length of 3.77 m, have a gravitational sag of about 800 μm when supported at the two ends in the horizontal position. The wires in the tubes have only 200 μm sag at their nominal tension of 350 g. In order to re-establish the centricity of the wires, the sag of the multi-layers can be corrected by the sag-adjustment system, which applies an adjustable force to the central cross-plate. Using the in-plane alignment system as reference, deformations can be corrected with a precision of about 10 μm. Thus, for each angle of installation in the ATLAS detector, the sag of drift tubes and wires can be matched, leading to wire

Table 6.3: Parameters of MDT barrel chambers. Numbers and dimensions (mm) of the tubes refer to the most common values. The special chambers have non-standard shapes to fit between magnet coils, support structures etc. The BIS.8 and BEE chambers have only one multi-layer. The BEE are located at the outer circumference of the end-cap cryostat and record tracks passing from the barrel to the end-cap.

Name	Layer	Standard chambers	Special chambers	Tube layers	Location in R	Tubes/ layer	Tubes total	Length along z	Width along ϕ	Spacer height
BIS	inner	96		2×4	4550	30	240	916	1820	6.5
BIS.7	inner		16	2×4	4550	30	240	916	1820	6.5
BIS.8	inner		16	1×3	4620	16	48	496	1000	—
BIL	inner	72		2×4	4949	36	288	1096	2820	170
BIM	inner		20	2×4	5373	36	288	1096	1685	170
BIR	inner		24	2×4	6056	36	288	916	1685	170
BMS	middle	72		2×3	8095	48	288	1497	3220	170
BMF	middle		12	2×3	8095	64	384	1937	3220	170
BML	middle	94		2×3	7139	56	336	1697	3700	317
BEE	middle		32	1×4	4415	48	192	1457	1060	—
BOS	outer	72		2×3	10569	72	432	2177	3920	317
BOF	outer		16	2×3	10675	64	384	2177	3920	317
BOG	outer		18	2×3	10675	40	240	1216	3920	317
BOL	outer	96		2×3	9500	72	432	2177	5110	317
Total		502	154							

Table 6.4: MDT chambers in the end-cap. In the region $1.3 < |\eta| < 2.4$, the EI, EM and EO chambers provide the three points for momentum measurement while in the transition region $1.0 < |\eta| < 1.3$ not covered by the EO wheel, the second and third points are provided by the EE and EM chambers (see figure 6.2). The EE chambers will only be installed in 2009. Dimensions are in mm. Values in columns 9–10 apply to the outermost trapezoidal chambers in each radial row.

Name	Layer	Chambers	Tube layers	Location in $\|z\|$	Radial chambers	Tubes/ layer	Tubes total	Radial length	Width along ϕ	Spacer height
EIS	inner	32	2×4	7261	2	36	288	1096	1745	121
EIL	inner	48	2×4	7675	4	54	432	1637	3295	121
EES	extra	32	2×3	10276	2	40	240	1216	2951	121
EEL	extra	30	2×3	11322	2	40	240	1216	4703	121
EMS	middle	80	2×3	13878	5	64	384	1937	3860	170
EML	middle	80	2×3	14294	5	64	384	1937	6008	170
EOS	outer	96	2×3	21424	6	48	288	1457	4202	170
EOL	outer	96	2×3	21840	6	48	288	1457	6503	170
Total		494								

centricity and circular symmetry of the drift field. This technique, however, is only applicable for the barrel chambers, while for the outermost end-cap chambers (EOL, EOS, EEL, and EES) they have been corrected for by construction.

The precision achieved in construction has been verified in cosmic ray tests and in the X-ray tomography facility operated at CERN. The result was an average deviation of the wire positions of ≤ 20 μm from the nominal over the full area of the chamber [184, 185].

Due to the tight construction tolerances and to the continued monitoring of global chamber deformations, the relative positions of MDT wires are sufficiently well known for the accuracy of a track segment in the 6 (8) tube layers to be limited only by the single-tube resolution (about 80 μm). Therefore, the resolution on the central point of a track segment in a 3 (4)-tube multi-layer is 50 (40) μm; combining the two multi-layers into a chamber yields an accuracy of 35 (30) μm. The relative positions of the chambers in radially-consecutive stations are monitored by the projective alignment system with a design accuracy of about 30 μm (section 6.5). For a track crossing three MDT chambers, a sagitta resolution of $\Delta S = 45$ μm is thus expected, corresponding to a momentum resolution $\delta p/p = \Delta S \times p/500$ μm, where p is given in units of TeV.

To monitor thermal deformation, each chamber carries from 3 to 28 temperature sensors, depending on chamber type, while the local magnetic field is monitored by two to four B-field sensors per chamber. Both environmental parameters are read out via the Detector Control System (DCS) (see section 8.5), in which each chamber represents a node.

An important design criterion in chamber construction is electrical integrity: low-impedance connections have to be provided between all metallic components. Because the bonds between most chamber components are epoxy glue, the gas bars, support structures and Faraday cages are connected with solid wire straps. The end-plugs of the tubes are screwed to a continuous metal plane (ground plane) which in turn is connected to the support structure. The Faraday cage which surrounds the electronics is made of thin aluminium sheets which have undergone a chemical treatment on the surface (chromatisation) to assure a conductive, unalterable surface.

To avoid ground loops among chambers, the kinematic mounts which slide on the rails have a ceramic inner surface, while non-conductive transition pieces are used to connect the gas bars to the external supplies. Care is also taken to isolate the readout of the in-plane alignment (RASNIK [186]) and the DCS from the chamber ground. After installation, the resistance between individual chambers and the ATLAS structure is typically > 1 GΩ. To assure a low-impedance connection to the safety ground, rows of chambers are connected to *one* common ground line, which, in turn, is connected to the ATLAS structure at a single point. A detailed account of final quality controls and chamber installation in the barrel is given in [187].

6.3.3 Signal path and readout electronics

The architecture of the MDT readout electronics chain is shown in figure 6.11. In the first stage, the raw tube signals are amplified, shaped and discriminated, eight tubes being served by one custom-designed monolithic ASD (Amplifier/Shaper/Discriminator) chip. The binary differential signals output by the ASD are routed to the Time-to-Digital Converter (TDC), where the arrival times of leading and trailing edges are stored in a large buffer memory together with an identifier of the corresponding tube and a flag indicating whether the edge is leading or trailing. The time is measured in units of the Timing, Trigger and Control (TTC) clock of 40.08 MHz, 12 bits being used for the beam-crossing identification and 5 bits for the subdivision of the 25 ns-period (fine time). The fine time period of 0.78 ns therefore leads to a RMS timing error of 0.23 ns corresponding to an average position error of about 5 μm. A detailed description of the MDT readout and of its components is given in [188–190].

2008 JINST 3 S08003

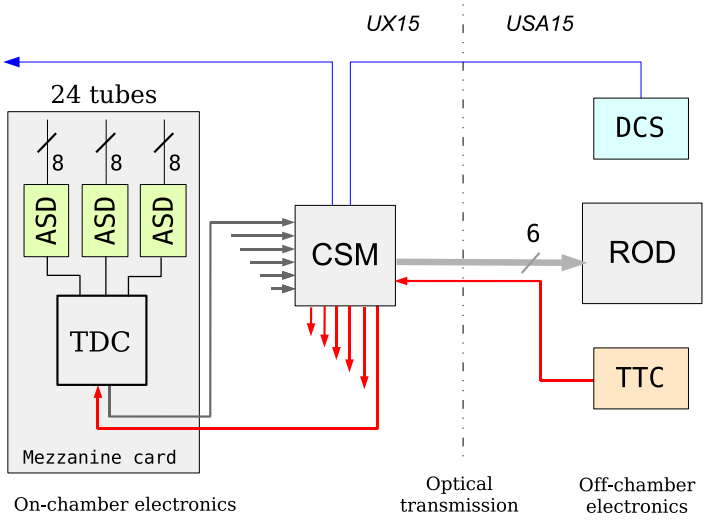

Figure 6.11: Schematic diagram of the MDT readout electronics. See text for details.

An additional feature of the ASD is the measurement of the pulse height of the signal, which allows the monitoring of the gas gain as well as pulse height dependent corrections (slewing corrections) [191]. The pulse height is measured by an Analogue-to-Digital Converter (ADC) and encoded as the delay between leading and trailing edge, a delay of 150 ns corresponding to the maximum pulse height to be recorded by the ADC. Thus the *trailing* edge of the ASD output is not determined by the discriminator status and does not contain any timing information. An internal dead-time disables the discriminator until after the pulse height encoding has safely elapsed. Beyond this minimum value, the dead-time is programmable and can be increased up to 750 ns in order to mask multiple hits from the same track. After the end of the dead-time, the first low-to-high transition of the discriminator will create the next leading edge of the ASD output. The standard dead-time setting will be 750 ns.

Programming of the ASD and TDC is done following the JTAG protocol via a shift register, allowing for a string of 54 bits for each ASD and a string of 180 bits for the TDC. This way, many parameters and functions can be controlled, like the setting of discriminator threshold and dead-time as well as triggering of test pulses for calibration or deactivation of noisy channels. The TDC with three ASD's, serving 24 tubes, is implemented on a 9×11 cm^2 printed circuit-board (mezzanine card). The mezzanine card is the basic readout element of the MDT's and is connected to the tubes via a signal distribution card (hedgehog board). There are about 15000 mezzanine cards to serve the 354000 MDT tubes in the system.

MDT chambers contain up to 18 mezzanine cards, which are controlled by a local processor, the Chamber Service Module (CSM), see figure 6.11. The CSM broadcasts the TTC signals to the TDC's and collects the hits they sent back for each L1 trigger (see section 8.2). Subsequently, the data are formatted, stored in a large derandomising buffer, and sent via optical link to the MDT Readout Driver (ROD) in the USA15 service cavern. The ROD is a VME module, serving up to six CSM's. Its main task is to format the front-end data for rapid transfer to the Readout Buffer

Table 6.5: Modularity of the MDT readout electronics. The difference between the number of chambers and CSM's in the barrel is due to each pair of BEE and BIS.8 chambers being served by only one CSM. The allocation of ROD's to the barrel or end-cap is approximate, some ROD's serving CSM's from both regions. See the text for definition of the acronyms.

Region	Tubes	ASD's	Mezzanine cards	CSM's	Chambers	ROD's
Barrel	191568	24114	8038	624	656	110
Two end-caps	162816	20352	6784	494	494	94
Total	354384	44466	14822	1118	1150	204

(ROB), where data are stored until the event has been either validated or discarded by the L2 trigger logic. Table 6.5 summarises the modularity of the readout system.

An important feature of the ROD is large processing power, which allows it to monitor the incoming data. The data stream received from the CSM's can be sampled for tube and chamber occupancies and their deviations from nominal values, possibly pointing to a malfunction. As the ROD's see the full L1 event rate, they can accumulate significant statistics in a short time, allowing for an early recognition of errors. Depending on average event size and L1 rate, a variable fraction of the events will be monitored in order to not slow down data transfer to the ROB's, which has priority. A detailed description of the MDT readout is given in [192] and [193].

6.3.4 Performance of the MDT chambers

MDT chambers have been tested under various conditions, trying to match the environment of the final experiment as closely as possible.

A set of 12 MDT chambers were tested in a high-energy muon beam in 2003 and 2004 in the H8 area at CERN. Six barrel MDT's (two of each type of BIL, BML, BMS chambers) were arranged as a barrel projective tower part of a large sector. Six end-cap MDT's were arranged to reproduce a projective region formed by one large and one small adjacent chambers in each of the EI, EM and EO stations. The main purpose was to verify the functionality and performance of the readout electronics and the projective alignment system. The resolution dependence on thresholds and gas gain was tested as well as efficiency and noise rates. The alignment system was used to monitor the chamber positions relative to each other recording, for example, day-night displacements of the chambers due to temperature. The optical alignment and the track alignment with the MDT's demonstrated the expected correlation with an accuracy 20 μm. These test-beam data were also used to develop the calibration algorithms measuring the space-time relation and to correct for the time offsets of the individual tubes. The calibration procedure is described in [174].

In 2004, tests were performed with the muon trigger chambers and with other sub-systems like the pixel detector, SCT, TRT, and the calorimeters. The main result was a confirmation of the performance with respect to the resolution parameters, readout functionality and stability of the electronics as well as the correct functioning of the alignment system. The results of the tests in 2003 and 2004 are presented in [181, 194, 195].

Additional tests were done in 2003/2004 at the Gamma Irradiation Facility (GIF) at CERN to test the behaviour of the chambers in a high background environment as is expected in the ATLAS hall. In the GIF test area, a high-energy muon beam was available as well as an adjustable, intense γ-source. The muon tracks were defined by a silicon telescope and the resolution of the MDT tubes could be studied accurately as a function of the γ-intensity and of the track's distance from the central wire. The expectation was that electrons from Compton scattering in the tube walls would lead to high occupancies, while positive ions, slowly drifting towards the wall, would locally distort the drift field, leading to a radius-dependent degradation of the resolution. Tests done in 1999 [170] on a few tubes, and in 2003 and 2004 on full chambers using final electronics [171, 172], demonstrated the feasibility of using Ar/CO_2 as the drift gas. Figure 6.12 shows the most recent results. The degradation of resolution with gamma intensity is clearly visible and is highest for the longest drift path close to the wall ($R = 15$ mm). The highest irradiation level expected for MDT chambers will result in ≤ 150 hits/(cm^{2}s). In the centre of the drift range of the tube ($R = 7.5$ mm) this would degrade the resolution from 60 μm to about 80 μm, which is acceptable.

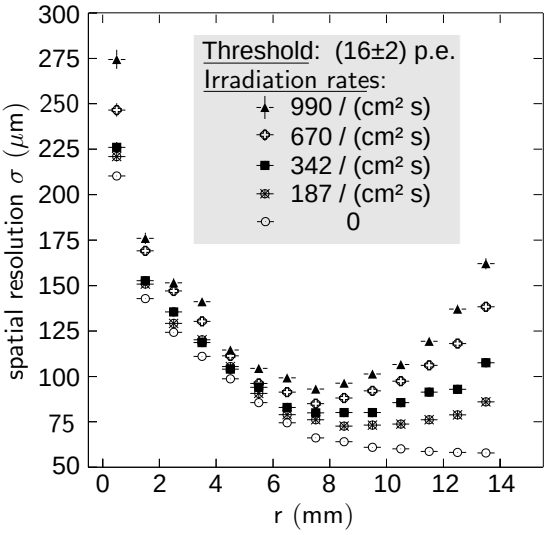

Figure 6.12: Resolution as a function of the impact parameter of the track with respect to the tube wire at various levels of hit rates induced by γ-irradiation. The threshold was 16 photoelectrons (p.e.). The maximum rate expected for the MDT's is ≤ 150 hits/cm^{2}s.

6.4 Cathode-strip chambers

6.4.1 Layout of the CSC system

The limit for safe operation of the MDT's is at counting rates of about 150 Hz/cm^2, which will be exceeded in the region $|\eta| > 2$ in the first layer of the end-cap. In this η region of the first layer, the MDT's are replaced by cathode-strip chambers, which combine high spatial, time and double track resolution with high-rate capability and low neutron sensitivity. Operation is considered safe up to counting rates of about 1000 Hz/cm^2, which is sufficient up to the forward boundary of the muon system at $|\eta| = 2.7$.

As in the case of the MDT's, the CSC's are segmented into large and small chambers in ϕ. The whole CSC system consists of two disks with eight chambers each (eight small and eight large) as shown in figure 6.13. Each chamber contains four CSC planes resulting in four independent measurements in η and ϕ along each track.

The CSC's are multiwire proportional chambers with the wires oriented in the radial direction (i.e. wires are parallel to the central wire, which points in the radial direction). Both cathodes are segmented, one with the strips perpendicular to the wires (providing the precision coordinate) and the other parallel to the wires providing the transverse coordinate. The position of the track is obtained by interpolation between the charges induced on neighbouring cathode strips. The CSC wire signals are not read out.

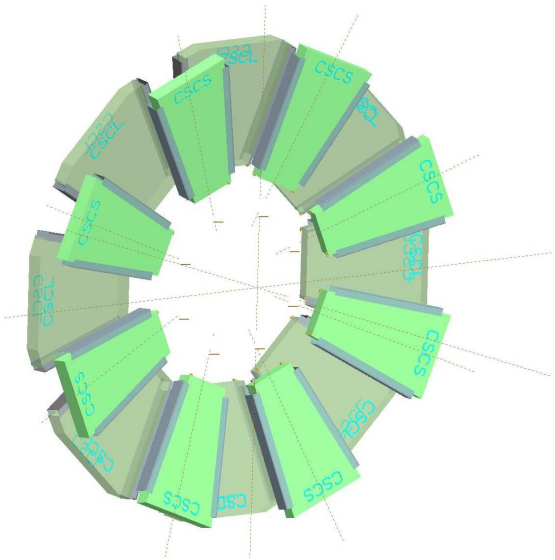

Figure 6.13: Layout of a CSC end-cap with eight small and eight large chambers.

The resolution achieved with this procedure depends on the signal-to-noise ratio and the readout pitch, the latter being the main cost-driving factor for the readout electronics. With a readout pitch of 5.31 mm and 5.56 mm for the large and small chambers respectively in the bending direction, the CSC reaches a resolution of 60 μm per CSC plane, to be compared with the 80 μm resolution of a MDT tube layer. In the non-bending direction the cathode segmentation is coarser leading to a resolution of 5 mm.

Apart from the precision and relative simplicity of the coordinate determination, there are a number of other characteristics which make the CSC's suitable for regions of high particle densities:

(a) Good two-track resolution.

(b) Pairing of the measurements in the two coordinates via the pulse height to resolve the ambiguities if more than one track is present.

(c) Electron drift times of less than 40 ns resulting in a timing resolution of about 7 ns per plane.

(d) Low neutron sensitivity because of the small gas volume and the absence of hydrogen in the chamber gas (Ar/CO_2).

Detailed information on chamber parameters is available in [176]. The operating parameters of the CSC are shown in table 6.6.

Table 6.6: Operating parameters of the CSC's.

Parameter	**Value**
Operating voltage	1900 V
Anode wire diameter	30 μm
Gas gain	6×10^4
Gas mixture	Ar/CO_2 (80/20)
Total ionisation (normal track)	90 ion pairs

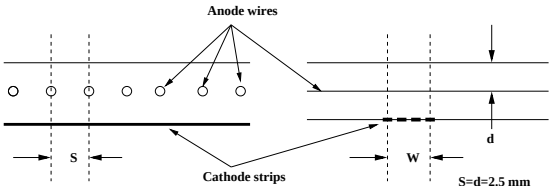

Figure 6.14: Left: structure of the CSC cells looking down the wires. The wire pitch s is equal to the anode-cathode spacing $d = 2.5$ mm. Right: view in the perpendicular direction (bending plane), down the readout and intermediate strips. The induction of the avalanche is spread out over 3–5 readout strips (see figures 6.15 and 6.16).

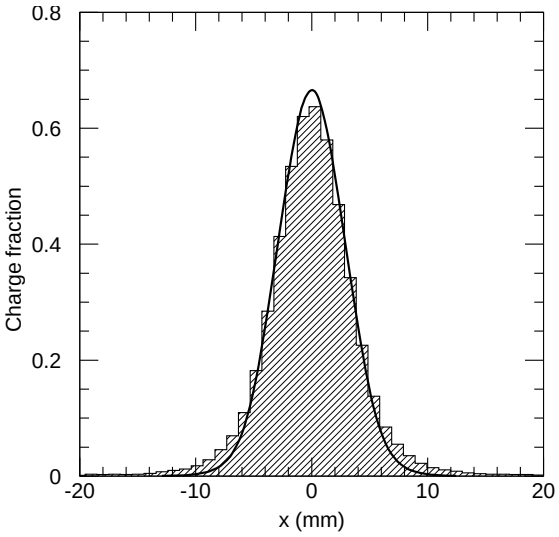

Figure 6.15: Charge distribution on the CSC cathode induced by the avalanche on the wire.

6.4.2 Spatial and time resolution

Figure 6.14 shows the symmetric cell structure of the CSC, the anode-cathode spacing being equal to the anode-wire pitch. The measured charge distribution as induced onto the cathode strips by the avalanche on the wire is given in figure 6.15.

The segmentation of the cathode aims to sample the induced charge distribution as precisely as possible while limiting the number of electronic readout channels. The following scheme has been chosen: between two neighbouring readout strips (connected to amplifiers) there are two intermediate (floating) strips capacitatively coupling the induced signal to the readout strips. The additional charge interpolation provided by the capacitive coupling reduces the differential non-linearity of the position measurement to $\leq 1\%$. Figure 6.16 shows the segmentation of the CSC cathode where for the large and small chambers the individual strip widths are 1.519 mm and 1.602 mm respectively, and the interstrip gap is 0.25 mm, resulting in readout pitches of 5.308 mm and 5.567 mm. The interstrip capacitance is about 10 times the strip capacitance to ground. The intermediate strips are connected to ground via a high-resistance path to define the DC potential.

As the precision coordinate in a CSC is obtained by the *relative* measurement of charges induced on adjacent strips, the performance is immune to the variation of conditions encountered by the whole chamber, like gas gain, temperature variations or pressure. The primary limiting factor for the spatial resolution of the CSC's is electronic noise of the pre-amplifiers, and therefore only a small number of strips around the centre is used in the clustering algorithm. In this geometry, the best results are obtained with 3 to 5 strips around the peak of the distribution.

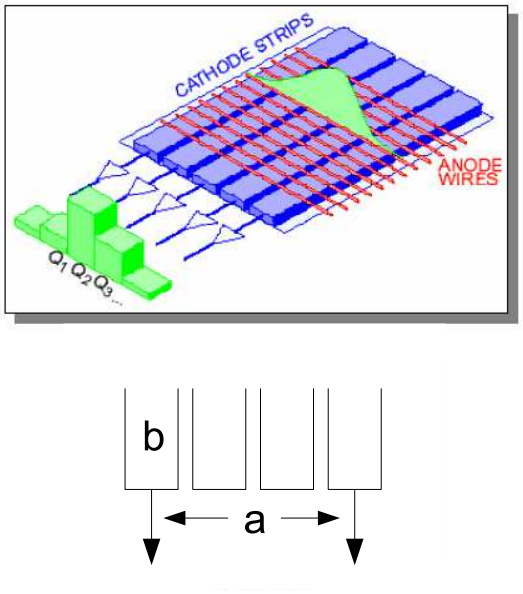

Figure 6.16: The segmentation of the CSC cathodes. The individual strip widths for the large and small chambers are $b = 1.519$ mm and 1.602 mm, respectively. The interstrip gap is 0.25 mm, resulting in readout pitches of $a = 5.308$ mm and 5.567 mm. The intermediate strips contribute an additional charge interpolation, improving the linearity of the reconstructed position. The intermediate strips are not connected to readout electronics.

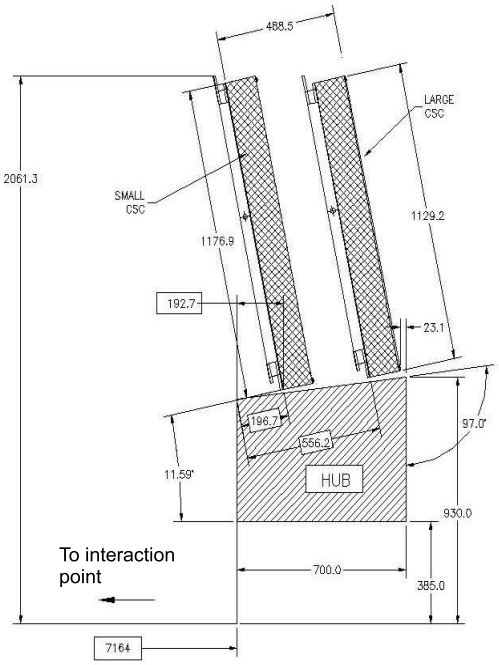

Figure 6.17: The inclination of the CSC's towards the interaction point. Dimensions are given in mm.

The second most significant contribution to the spatial resolution of the CSC is the effect of inclined tracks and the Lorentz angle. The charge interpolation is optimal when the avalanche is formed on a single point along the wire, while a significant extent of the anode charge results in a degradation. The spreading of the charge deposition can be caused by delta electrons, inclined tracks and a Lorentz force along the wire, as the magnetic field is not collinear with the electric field around the wire. While the effect of the Lorentz force cannot be corrected in a CSC, it does not lead to a systematic shift of the measured coordinate, but only to a slight reduction in resolution. The effect of inclined tracks is minimised by tilting the chamber towards the interaction point so that infinite momentum tracks are normal at the centre of the chamber (figure 6.17).

The strips in the second cathode plane are parallel to the wires and measure the position of the avalanche in the non-bending ϕ-plane. The spacing of the readout strips is larger than the one in the bending η-plane (21 mm and 12.92 mm for large and small chambers, respectively) leading to a resolution of about 5 mm.

2008 JINST 3 S08003

Table 6.7: Modularity of the CSC system and readout.

		Wires	Strips	Readout channels	Strips	Readout channels	Total readout channels	Front-end chips	Front-end boards
			along wires		across wires				
Plane	small	250	48	48	574	192	240	10	
	large	402	48	48	574	192	240	10	
Chamber	small	1000	192	192	2296	768	960	40	10
	large	1608	192	192	2296	768	960	40	10
One side	16 chambers	20864	3072	3072	36736	12288	15360	640	160
System	32 chambers	41728	6144	6144	73472	24576	30720	1280	320

If more than one track is present in a given event, the pulse height is used to match the measurements in the two projections. Because of the broad pulse height distribution in a gas chamber and the high resolution of the ADC's, both tracks will have, in most of the cases, a different pulse height value, allowing for an unambiguous η/ϕ assignment of the tracks from the separate measurements in η and ϕ. In the rare cases of near equality, the information from the other three chamber layers will be used. In using the information of all four chamber layers, the η/ϕ assignment for two or more tracks seems to be sufficiently robust.

The time resolution of the CSC is an important parameter for the correct tagging of the beam-crossing. The maximum drift path of a primary electron to the closest wire being only 1.27 mm, one would expect a maximum drift time of about 20 ns, given the average drift velocity of 60 μm/ns. However, the vanishing drift field at the boundary between two cells creates regions of very low drift velocity leading to long tails in the distribution of the arrival times, which prevents reliable tagging of the beam-crossing. By OR-ing the signals of corresponding cathode strips in the four chamber planes, the tails disappear, as virtually no track can pass close to a cell boundary in all four layers. The time of arrival distribution thus obtained is symmetric with an RMS value of 3.6 ns, resulting in a reliable tagging of the beam-crossing.

6.4.3 Mechanical design

The CSC's are located at a distance of about 7 m from the interaction point. They are mounted together with the MDT's and TGC's on the shielding disk (see section 3.2) forming the so-called small wheel and occupy the radial space between 881 mm and 2081 mm, corresponding to the pseudorapidity range $|\eta| = 2 - 2.7$.

The CSC's come in two types of chambers as shown in figure 6.18 and are arranged in two disks of eight chambers each, as shown in figure 6.13. Each chamber consists of four wire planes leading to a similar configuration like in the multi-layer of the MDT system, but with much finer granularity. The modularity of the CSC system is summarised in table 6.7.

The CSC design utilises low-mass materials to minimise multiple scattering and detector weight. A four layer chamber is formed by five flat rigid panels, each made of an 18.75 mm thick sheet of polyurethane foam and two 0.82 mm thick copper-clad laminates, where the 17 μm thick copper cladding forms the cathodes. Precision strips glued on the panels provide the 2.5 mm step for the anode wire plane. The anode wires have a diameter of 30 μm and are made of gold-plated tungsten with 3% rhenium.

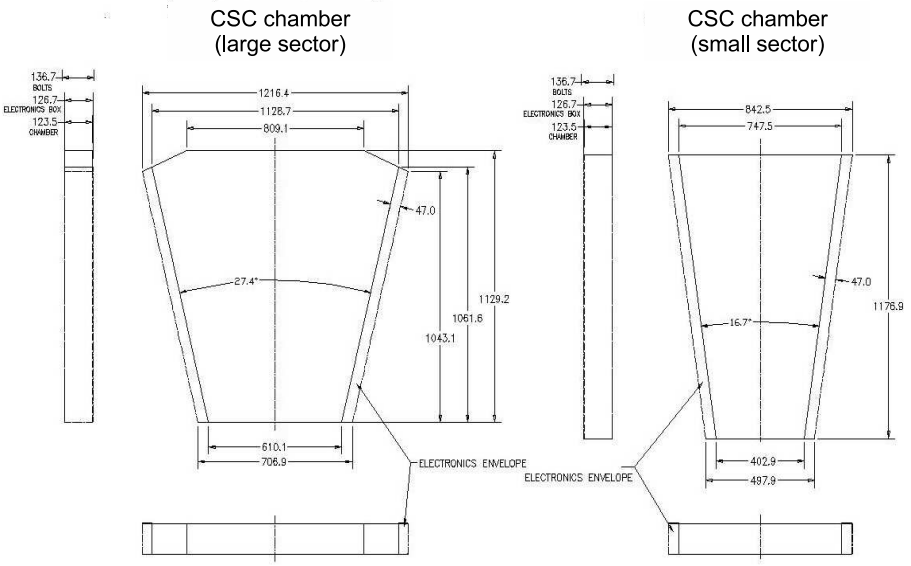

Figure 6.18: Shapes of large and small CSC's. Dimensions are given in mm.

There are 250 and 402 wires per chamber plane along the bending direction in the small and large chambers, respectively (table 6.7). The readout pitch in the bending plane is 5.56 mm and 5.31 mm for the small and large sectors respectively with a total of 192 channels per plane for both. The odd strip width is the result of the different radial chamber lengths and the desire to fix the number of channels in multiples of 192. The transverse coordinate strips have widths of 12.52 mm and 21.00 mm for the small and large chambers respectively with a total of 48 strips per plane. The cathode strips are lithographically etched for highest precision. The five panels are precisely positioned with respect to each other with the aid of locating pins. The outer copper-clad laminates of each chamber form an electromagnetic shield for the detector. A cutout view of one gap formed by two panels is shown in figure 6.19. Signals from the precision cathode strips are directly connected to the front-end (ASM-I) boards located on the chamber edges. The transverse coordinate signals are transferred via short ribbon cables to similar front-end boards mounted on the chamber frame (figure 6.20).

The 16 chambers of an end-cap are mounted onto precisely manufactured stainless steel frames which, in turn, are mounted on adjustable brackets of the small wheel structure.

6.4.4 Readout electronics

The CSC's have to operate at the innermost part of the small wheel, a region which is characterised by a high density of detector components, difficult accessibility and high radiation levels. As standard components like CMOS-processors, FPGA's or commercial ADC's are not expected to operate reliably in this environment, the readout electronics had to consist of custom-designed building blocks, fabricated in radiation hard technologies, combining performance with simplicity and reliability. All other commercial components were radiation certified according to ATLAS

2008 JINST 3 S08003

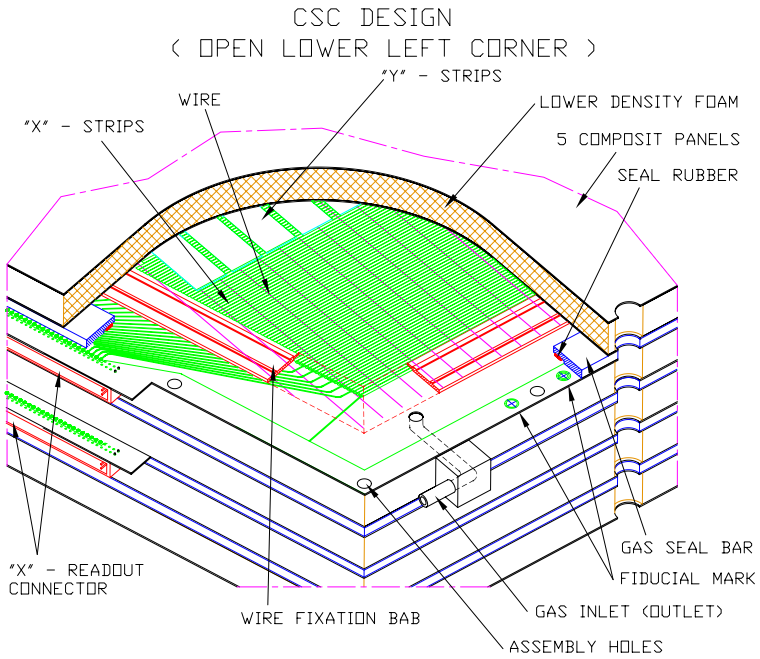

Figure 6.19: Structure of the CSC.

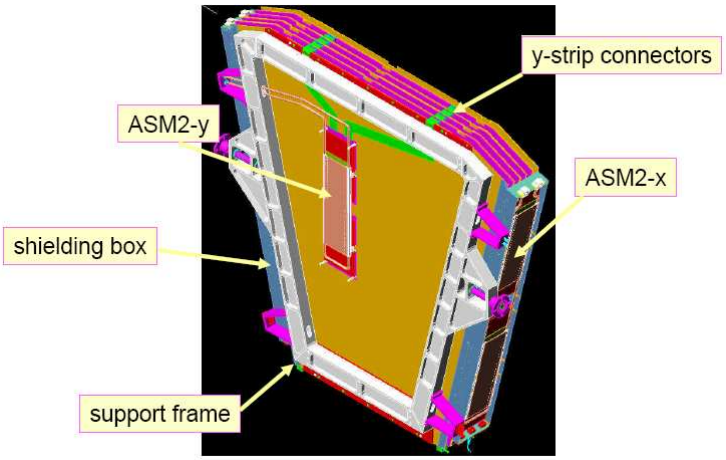

Figure 6.20: Model of a CSC chamber with four planes showing the location of the readout electronics.

requirements. To limit the number and complexity of custom components, the front-end functionality had to be reduced to a minimum. The design therefore aimed at shifting the data as early as possible, i.e. after the L1 trigger latency to the ROD's in the shielded area in USA15.

The readout architecture of the CSC's is shown in figure 6.21. At the first stage, the chamber signals are amplified and shaped (ASM-I). At the second stage, the pulse train is sampled at a rate of 40.08 MHz and is stored in a Switched Capacitor Array (SCA) while awaiting the L1 trigger

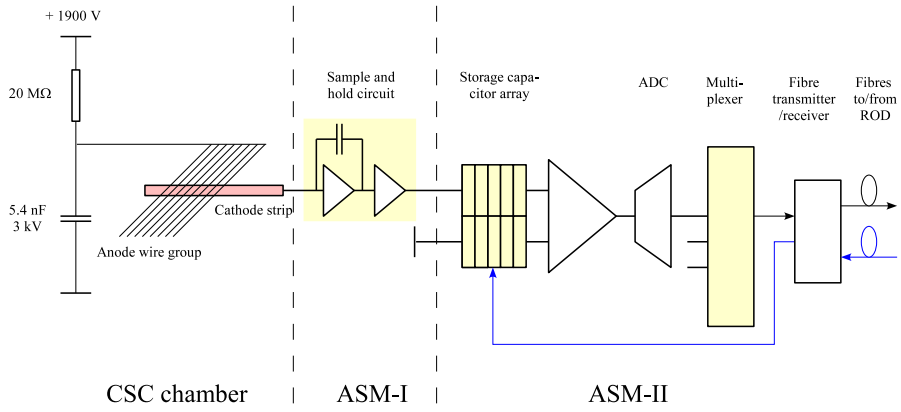

Figure 6.21: Schematics of the CSC front-end electronics. Regions shaded in yellow represent custom-made ASIC's.

decision. Upon arrival of a L1 trigger accept signal, the stored data are digitised, multiplexed and transferred to the ROD.

A particularly demanding aspect of the centroid-finding system is to achieve an intercalibration of $< 0.5\%$ between adjacent channels. This requires high stability of the front-end amplifiers and small leakage in the analogue storage system, as well as an appropriate calibration system.

Signal processing in the front-end chip, crucial for the system performance, is as follows. Subsequent to the charge-sensing pre-amplifier, the pulse-shaping stage consists of a seventh order filter providing a bipolar pulse with a 70 ns peaking time, to reject low-frequency noise and to assure a prompt return of the signal to the baseline. The choice of these parameters was based on an assumed maximum rate of about 600 kHz per strip at full LHC luminosity, including the usual safety factor of 5. Pre-amplifier and shaper are realised as monolithics with 24 channels per chip. The 0.5 μm CMOS technology was used because of known reliability and high radiation tolerance.

Each CSC chamber has 768 readout channels in the precision (bending) and 192 in the transverse direction, so 32 and 8 chips (24 channels) are needed for the readout of both directions, respectively. A group of four chips is mounted on a printed circuit-board (ASM-I), such that the 40 chips of a chamber are served by 10 ASM-I boards, which are mounted on the lateral frame of the CSC, see figure 6.20. Two ASM-I boards in turn are served by one ASM-II board which sends the signals to the off-detector electronics via optical fibres. A breakdown of components used in the CSC readout is given in table 6.7.

The signals from the ASM-II boards are routed to the CSC ROD's in the USA15 control room. The ROD's are VME modules which perform zero suppression, discard signals with incorrect timing, apply calibration constants and build event fragments to be sent to the TDAQ system. They also provide control signals for the on-chamber electronics. ROD's are interfaced to the front-end and to the TDAQ via transition modules which handle all data traffic via optical fibres.

Each ROD services two CSC's and consists of 13 DSP-based generic processing units, which communicate with the ASM-II's (10), build event fragments (2) and handle the operation of the ROD and the interface to the TDAQ (1). More details on the CSC readout are given in [196, 197].

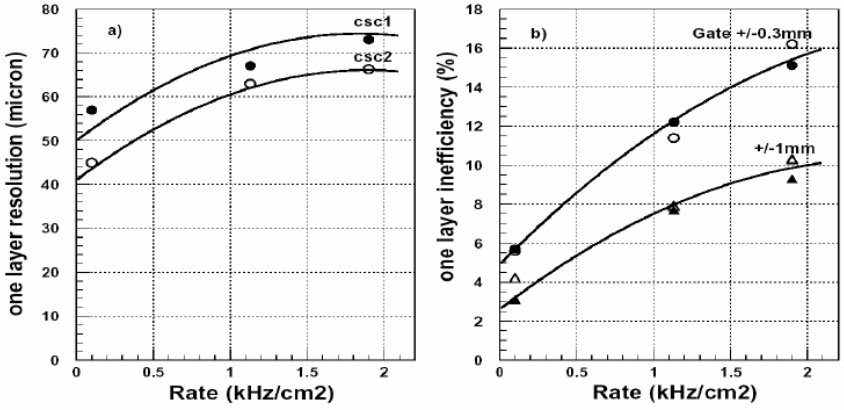

Figure 6.22: CSC resolution and efficiency in a high rate test.

An additional constraint for the construction of the readout system came from the fact that natural air convection is practically absent around the CSC's, and so liquid cooling had to be provided to evacuate the dissipated heat. Water cooling is implemented for the front-end electronics of the CSC's, using the leakless cooling technique developed for CERN experiments.

6.4.5 Performance of the CSC

The CSC's have been tested under conditions as close as possible to those in the final experiment. For this, the Gamma Irradiation Facility at CERN has been used. In any tested chamber of four CSC planes, two layers were used as reference for the track location while the other two were considered the devices under investigation. The intensity of the gamma background could be adjusted up to 2 kHz/cm^2. The results are shown in figure 6.22. Compared to zero background, the resolution degrades from ~ 45 μm to 65 μm at 1 kHz/cm^2, while the inefficiency of a single CSC layer increases from $\sim 4\%$ to 10%. The 10% inefficiency at 1 kHz/cm^2 is acceptable, as the probability for two or more layers to be inefficient in the same event is very low.

6.5 Alignment system of the precision chambers

In the ATLAS spectrometer, the MDT as well as the CSC chambers and their auxiliary alignment objects (alignment bars and reference system plates, see below) are installed with a precision of about 5 mm and 2 mrad with respect to their nominal positions. In contrast, the actual chamber locations must be known to a precision of $\leq 30\,\mu$m in order to achieve the required momentum resolution: this is more than two orders of magnitude tighter than the positioning accuracy. To reach this precision goal, an alignment system was built which relates the position of each chamber to that of its neighbours, both within an MDT layer and along $R-z$ trajectories within MDT towers. With the internal accuracy of the MDT's guaranteed by construction, and their planarity monitored by optical in-plane alignment sensors (see section 6.3.2), this alignment system forms a dense, stable grid for monitoring (in the barrel) or reconstructing (in the end-cap) the position of each MDT wire in the muon system. A schematic representation of the alignment system in a large

2008 JINST 3 S08003

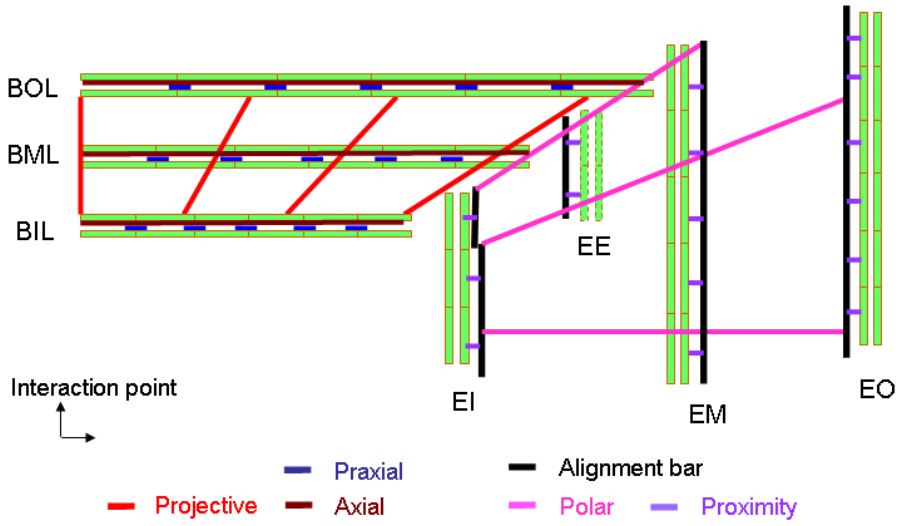

Figure 6.23: Principle of the alignment of the ATLAS muon spectrometer. See text for details.

sector is shown in figure 6.23. Due to different geometrical constraints, the alignment strategies are somewhat different in the barrel and end-cap regions (section 6.5.1) and several specialised optical alignment sensors have been developed (section 6.5.2). The overall system layout is detailed in section 6.5.3.

The optical alignment techniques described below are insufficient to reconstruct, on their own, the absolute positions of the MDT barrel chambers: only variations in relative position can be determined with the required precision. Track-based alignment algorithms must therefore be used in combination with the optical system to achieve the desired sagitta accuracy, and also to determine the global positions of the barrel and end-cap muon-chamber systems with respect to each other and to the inner detector, in the overall ATLAS reference frame (section 10.3.2). A more extensive presentation of the alignment strategy and technical implementation can be found in [198, 199].

6.5.1 Alignment strategies

In the barrel, the chambers inside a MDT row are referenced to each other by chamber-to-chamber alignment sensors (praxial and axial systems, see figure 6.23), while the projective system connects the inner, middle, and outer MDT layers, simulating the trajectories of an infinite-momentum track originating from the interaction point. This optical network is able to reliably detect relative changes in chamber position at the 20 μm level. However, because of its essentially projective configuration, it remains insensitive to some specific geometrical distortions, and therefore unable to provide absolute chamber positions on its own. Additional optical lines (table 6.8) link MDT chambers to the barrel toroid cryostat, or relate adjoining chambers in large and small sectors. Once fully functional, the optical alignment system will provide a slightly overconstrained network of optical sensors which can determine the absolute chamber positions in the barrel region to an accuracy of a few hundred microns, and yield a systematic uncertainty of 100 – 200 μm on

Table 6.8: The alignment components in barrel and end-cap. Three different types of imaging systems are used, adapted to the special application: RASNIK (R), BCAM (B) and SaCam (S). The BIR and BIM chambers are shown in figure 6.1. See text for details.

Barrel alignment				**End-cap alignment**			
Name	Type	Number	Function	Name	Type	Number	Function
In-plane	R	2110	MDT deformation	In-plane	R	1984	MDT deformation
Praxial	R	2006	MDT-MDT distance	In-bar	R	352	Bar deformation
Axial	R	1036	MDT-MDT planarity	Radial	B	96	Bar deformation
Projective	R	117	Tower alignment	Polar	B	208	Bar-bar link
Reference	S	256	Link to toroid	Azimuthal	B	736	Bar-bar link
CCC	S	260	Small-large link	Proximity	R	2384	MDT-bar and MDT-MDT link
BIR-BIM	R	32	BIR/BIM link	Saloon door	B	584	MDT-bar link
				3D sensor	B	192	CSC-bar and CSC-CSC link
Total:		5817		Total:		6536	

the residual sagitta. Because of mechanical positioning uncertainties on some optical sensors, the ultimate 30 μm precision on the sagitta (but not necessarily on the absolute chamber positions), and in particular the exact reference values with respect to which relative changes are monitored, can only be reached, in the barrel region, by combining optical and track-based alignment algorithms.

In the end-caps, the light path between the inner and the middle layer is obstructed by the cryostat vessels of the toroid magnets. The polar alignment therefore proceeds in two steps using high-precision rulers (alignment bars), as an intermediate reference [200]. The polar (quasi-projective) optical lines connect the alignment bars installed in each EI, EM and EO layer; the chambers, in turn, are optically connected to their neighbouring bars by proximity sensors. Additional sensor families, listed in table 6.8, determine the remaining degrees of freedom. Simulations have demonstrated that this network is sufficiently precise and overconstrained to determine absolute chamber positions within each end-cap region to a 300 μm accuracy, and relative chamber positions along muon trajectories to a 40 μm accuracy on the sagitta. Test-beam results and preliminary tests after installation of the EM layers in the ATLAS cavern have already demonstrated that an alignment accuracy at about this level is reached.

The alignment bars in the EI wheel are also used for the alignment of the CSC's. The positions of the large CSC's relative to these bars and the position of the small CSC's relative to the large ones are measured with optical sensors, in a similar way as is done for the MDT's. The alignment precision of the CSC's is thus expected to be at the same level as for the MDT's.

The relative positions of the barrel MDT system and of the forward end-cap chamber systems must also be known to a few tens of microns to ensure accurate momentum measurement for muons crossing from one region to the other. Track-based alignment algorithms are being developed to provide the required precision.

6.5.2 Optical alignment sensors

Three different optical systems are used in the ATLAS alignment: RASNIK's, BCAM's and SaCam's. All three systems are based on the principle of a three point straightness monitor: an optoelectronic image sensor (CCD or CMOS) monitors the position of an illuminated target through

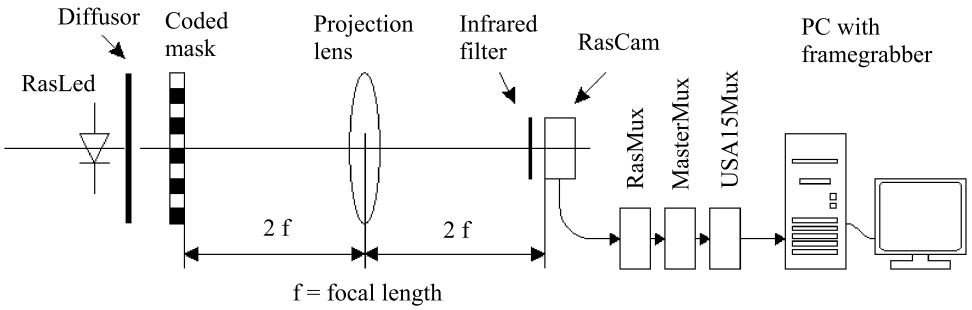

Figure 6.24: The RASNIK alignment system. The image sensor (RasCam) is a CMOS sensor in the barrel and a CCD sensor in the end-cap. An infrared filter is placed in front of the sensors to avoid stray light. A RasMux multiplexer is installed on each chamber, servicing up to eight RasCam sensors. A MasterMux can multiplex up to 16 RasMux's, sending the data to the USA15 hall for processing.

a lens. The sensor image is analysed online and converted into four parameters characterising the deviation from the nominal geometry: two translations perpendicular to the optical axis, the rotation around and the longitudinal position along the axis, the latter being derived from the optical magnification.

Figure 6.24 shows a schematic of the RASNIK system, the most frequently used element of the muon alignment system. An image sensor (RasCam) monitors through a lens an illuminated target carrying a chequer-board pattern imprinted on a mask. For a symmetric RASNIK with the lens halfway between image sensor and mask, a transverse resolution of 1 μm and a magnification resolution of 2×10^{-5} have been obtained. A description of the RASNIK alignment system can be found in [186] and [201].

The BCAM is a camera consisting of a CCD image sensor which monitors the position of a laser diode through a lens. The BCAM housing also contains a set of two or four laser diodes which can be used as targets by another BCAM. BCAM's are mostly used in pairs, facing each other. The image sensor is placed close to the focal plane of the lens (76 mm), while the target with the laser diodes is placed at a distance of 0.5 m to 16 m. The image of a laser diode on the CCD appears as a circular spot.

BCAM's achieve a resolution of 5 μrad for a target distance of 16 m. If the target consists of two or more laser diodes with a known separation, relative angles can be extracted, which yield magnification and rotation around the optical axis. If BCAM's are used in pairs, the absolute angular position of the partner can be determined with 50 μrad accuracy.

Like the BCAM, the SaCam consists of a camera with an image sensor and a lens at fixed distance. The target consists of four back-illuminated holes, covered by a light diffuser. The lens is mounted at distances ranging from 25 mm to 80 mm, depending on the distance between image sensor and target. A relative resolution of 5 μrad has been achieved with the SaCam, a result similar to that of the BCAM.

Another specialised sensor type is the 3D sensor, a pin-hole camera similar to the BCAM, which monitors the position of four laser diodes placed at two different distances along the optical axis. This sensor type is used for the alignment of the CSC's.

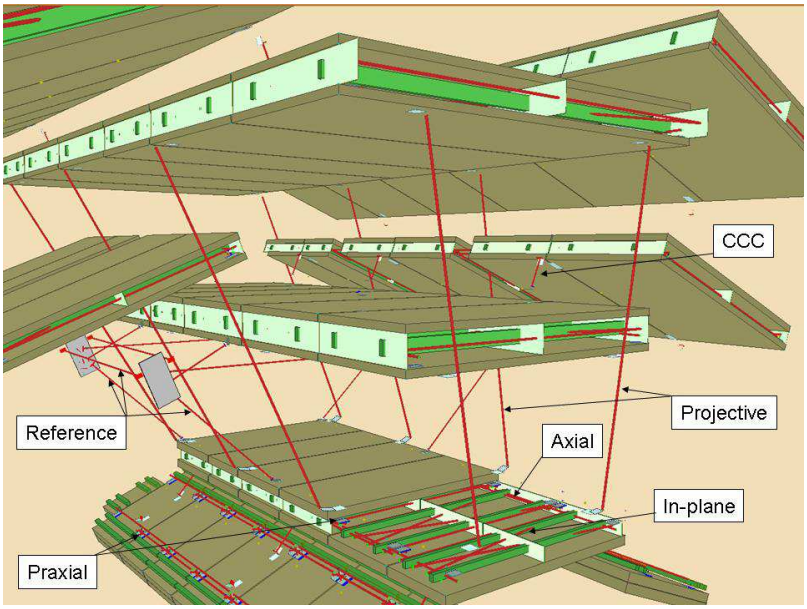

Figure 6.25: Layout of the optical-alignment lines (red) for three adjacent barrel sectors. See text and table 6.8 for details. The Chamber-to-Chamber Connector sensors (CCC) connect chambers in a small sector to those in an adjacent large sector.

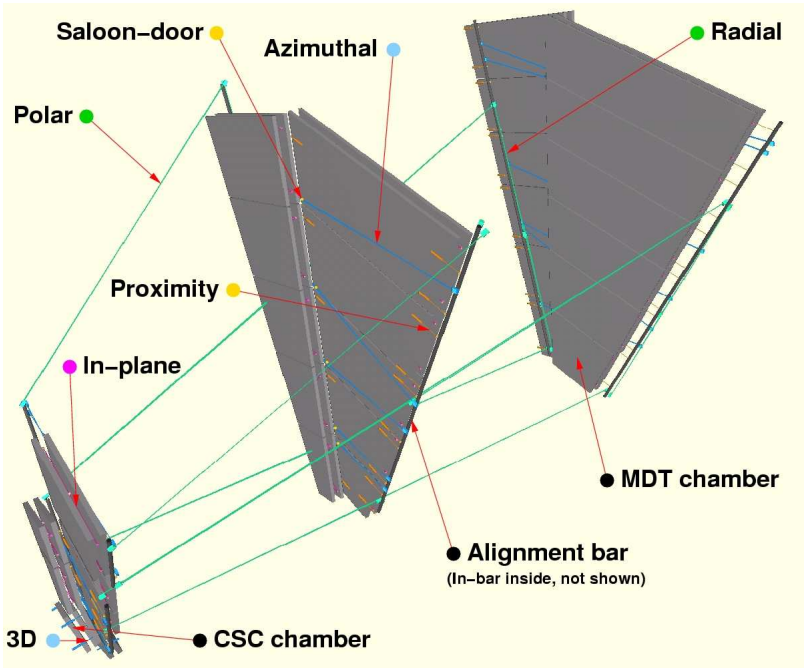

Figure 6.26: Layout of the alignment of two MDT's and CSC's in the end-cap. Only alignment sensors belonging to these sectors are shown, and the EE chambers and bars have been omitted. See text and table 6.8 for details.

2008 JINST 3 S08003

6.5.3 Layout of the alignment system

The alignment rays in three adjacent barrel sectors are shown in figure 6.25. The praxial systems (two short, crossed RASNIK's connecting adjacent chamber corners) and the axial systems (interleaved long RASNIK systems along the chamber) monitor the geometry of each row of six chambers. The relative position of the chamber layers perpendicular to the polar direction is monitored by the projective rays. The projective system works with RASNIK's, where BIL chambers hold the mask, BML's the lenses and BOL's the image sensor. Chambers in the small sectors (BIS, BMS and BOS) are not equipped with projective lines and are referenced to the adjacent large chambers by Chamber-Chamber Connection sensor (CCC).

The layout of the alignment rays in the end-cap is shown in figure 6.26. The presence of the cryostat of the end-cap toroid magnet allows only for three polar lines per small sector, one of them passing through a horizontal stay tube connecting the two outer flanges of the cryostat. To cope with this limitation, a grid of alignment bars using a quasi-projective alignment system was built. The chamber positions are referenced to this grid of aligned precision rulers. Each MDT wheel carries eight bars, with lengths of up to 9.6 m, placed at the border between large and small sectors. The bar straightness and elongation are monitored by a set of internal, interleaved RASNIK's and by a number of temperature sensors. Prior to installation, the geometry of each bar is carefully measured using a large coordinate measuring machine.

The bar positions in the grid are determined by a network of BCAM sensors measuring the bearing angle of light sources located on adjacent bars. Radial BCAM's monitor the bar deformation, azimuthal BCAM's connect adjacent bars within a wheel, and polar BCAM's connect bars of different wheels. MDT chambers are referenced to the alignment grid using RASNIK proximity sensors, where image sensor and lens are placed on the chamber, while the mask is on the neighbouring bar. In order to monitor chamber rotations around the bar axis, azimuthal BCAM's also look at targets (the saloon-door sources) on the opposite edge of the adjacent MDT chamber. The positions of CSC chambers relative to the bars and to each other are measured by 3D sensors.

6.6 Trigger chambers

The trigger chambers of the muon system provide fast information on muon tracks traversing the detector, allowing the L1 trigger logic to recognise their multiplicity and approximate energy range. The main requirements for the trigger system are:

- discrimination on muon transverse momentum;
- bunch-crossing identification;
- fast and coarse tracking information to be used in the high-level trigger stages;
- second coordinate measurement in the non-bending ϕ-projection to complement the MDT measurement, see section 6.2;
- robustness towards random hits due to n/γ-background in the experimental hall.

The trigger detectors must provide acceptance in the range $|\eta| \leq 2.4$ and over the full ϕ-range. This poses a considerable challenge to the design of the trigger system as resolution requirements in barrel and end-cap are quite different, an obvious reason being that muon momenta, corresponding to a given p_T, are strongly increasing with η. At $|\eta| = 2.4$, for example, p is about 5.8 times larger than p_T, while the integrated bending power is only about twice the value as at $\eta = 0$. This leads to the necessity of an increased and η-dependent granularity in the end-cap trigger system, if the p_T-resolution is to match the one in the barrel. The fact that the three trigger layers in the end-cap are outside the magnetic field, seeing no curvature, and that their respective distances are smaller than the ones in the barrel (figure 6.27) also calls for a finer granularity of the end-cap trigger readout. Furthermore, radiation levels in the end-cap region reach a factor of 10 higher than in the barrel. Another difficulty for end-cap triggering comes from the strong inhomogeneities of the magnetic field in the region $1.3 \leq |\eta| \leq 1.65$ as can be seen in figure 2.10. In this transition region, the superposition of the fields of barrel and end-cap toroids leads to a complex field geometry with large field components in ϕ (the non-bending plane) and strong inhomogeneities of the integrated bending power, which in two locations in the η and ϕ plane is close to zero. In this angular region, all tracks are nearly straight, similar to tracks with very high momentum. In order to avoid high fake trigger rates, this region can be excluded from the trigger by a masking algorithm, which again calls for a fine readout granularity to keep the resulting trigger losses to a minimum.

Taking these constraints into account, two different technologies have been selected for barrel ($|\eta| \leq 1.05$) and end-cap ($1.05 \leq |\eta| \leq 2.4$) regions. In the barrel, Resistive Plate Chambers (RPC's) are used due to good spatial and time resolution as well as adequate rate capability. A RPC has no wires, which simplifies its construction and makes chambers less sensitive to small deviations from planarity if appropriate spacers are used to keep the gap width constant. Being located in the comparatively homogeneous field of the barrel toroid and having sufficient spacing between the three trigger layers (see table 6.9), RPC's give sufficient trigger selectivity even with moderate channel count, i.e. spatial resolution.

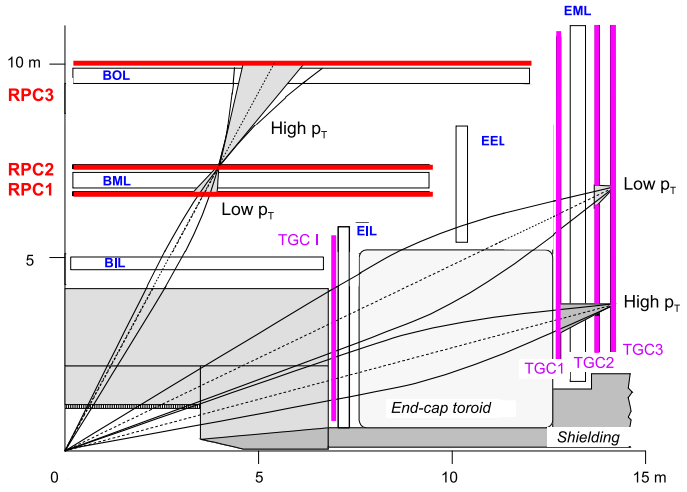

Figure 6.27: Schematics of the muon trigger system. RPC2 and TGC3 are the reference (pivot) planes for barrel and end-cap, respectively.

In the end-cap region, Thin Gap Chambers (TGC's) have been selected: they operate on the same principle as multi-wire proportional chambers, and they provide good time resolution and high rate capability. Their spatial resolution is mainly determined by the readout channel granularity, which can be adjusted to the needs by wire ganging. TGC's have demonstrated a high level of reliability and robustness in previous experiments.

To reduce the probability of accidental triggers caused by random combinations of converted γ's, the coincidence condition in both types of trigger chambers is established separately in the η

Table 6.9: Segmentation of the RPC system in 544 chambers and 962 units (126 chambers are made of only one unit). Columns 4 and 9 give the radial positions of the RPC stations, while columns 5 and 10 give the distance to the pivot station (RPC2), relevant for the p_T resolution. All dimensions are in mm.

	Small sector					Large sector				
Name	**Units**	**Chambers**	**Location in R**	**To pivot**	**Maximum $\|z\|$**	**Units**	**Chambers**	**Location in R**	**To pivot**	**Maximum $\|z\|$**
RPC1	148	84	7820	545	9362	149	94	6800	678	9147
RPC2	148	84	8365		9362	149	94	7478		9660
RPC3	176	92	10229	1864	12847	192	96	9832	2354	12267
Total	472	260				490	284			

and ϕ-projection, a valid trigger requiring a coincidence of both. This also suppresses fake triggers from curling tracks, i.e. multi-MeV electrons from γ-conversions, spiralling in the magnetic field, potentially creating correlated hits in the trigger chambers. In the barrel, three layers of trigger chambers are implemented while in the end-cap a forth layer is added to increase the trigger robustness in case of higher backgrounds. The schematic layout of the trigger system is shown in figure 6.27. In the barrel, two layers (RPC1 and RPC2) sandwich the MDT's of the middle layer, while the third one (RPC3) is located close to the outer MDT layer. In the end-cap, the three layers are in front (TGC1) and behind (TGC2 and TGC3) the second MDT wheel, while the fourth layer is located in front of the innermost tracking layer. The trigger information is generated by a system of fast coincidences between the three last layers along the trajectory of the muon particle. Each coincidence pattern corresponds to a certain deviation from straightness, i.e. curvature of the track, which is used as a criterion for the track to have passed a predefined momentum threshold.

The deviation from straightness is the deviation of the slope of the track segment between two trigger chambers from the slope of a straight line between the interaction point and the hit in a reference layer called the pivot plane, which is the second layer in the barrel (RPC2) and the last layer in the end-cap (TGC3), as illustrated in figure 6.27. For the low (high)-p_T trigger in the barrel, for example, the slope between RPC2 and RPC1 (RPC3) is compared to the slope between the interaction point and RPC2.

To assure full acceptance down to the low-momentum limit, the trigger chambers have regions of overlap with adjacent chambers and between the barrel and end-cap regions. As this may cause double counting of tracks leading to fake two-muon triggers, algorithms are in place to treat these overlap regions, either within the barrel or end-cap trigger logic, or as a part of the muon interface to the central trigger processor, see section 8.2.2.3. An overview of the muon trigger chambers is given in [202, 203] and details about the coincidence system and readout logic are given in [204].

6.7 Resistive plate chambers

The trigger system in the barrel consists of three concentric cylindrical layers around the beam axis, referred to as the three trigger stations. Figure 6.28 shows a standard barrel sector and the location of the RPC's (coloured) relative to the MDT's. The large lever arm between inner and outer RPC's permits the trigger to select high momentum tracks in the range 9–35 GeV (high-p_T trigger), while the two inner chambers provide the low-p_T trigger in the range 6–9 GeV. The chamber count and radial position of the RPC's are given in table 6.9. Each station consists of two

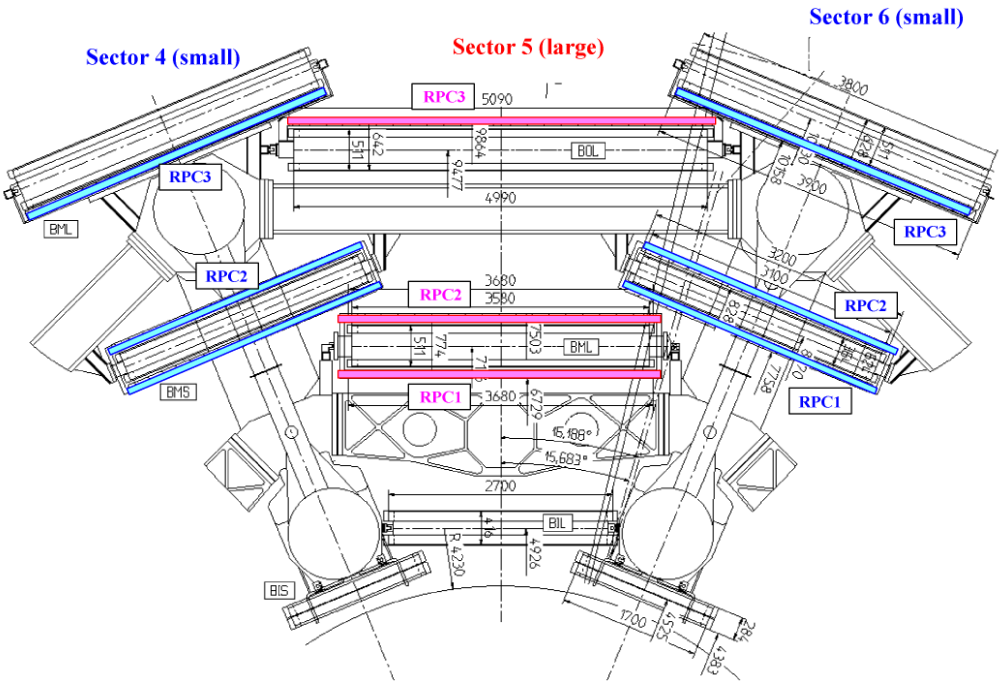

Figure 6.28: Cross-section through the upper part of the barrel with the RPC's marked in colour. In the middle chamber layer, RPC1 and RPC2 are below and above their respective MDT partner. In the outer layer, the RPC3 is above the MDT in the large and below the MDT in the small sectors. All dimensions are in mm.

independent detector layers, each measuring η and ϕ. A track going through all three stations thus delivers six measurements in η and ϕ. This redundancy in the track measurement allows the use of a 3-out-of-4 coincidence in both projections for the low-p_T trigger (RPC1 and RPC2 stations) and a 1-out-of-2 OR for the high-p_T trigger (RPC3 station). This coincidence scheme rejects fake tracks from noise hits and greatly improves the trigger efficiency in the presence of small chamber inefficiencies.

The naming scheme of the RPC's is identical to the one in the MDT's, a RPC in a small sector of the middle layer thus being called a BMS. To denote a RPC/MDT pair in the outer layer the term station is used, while for the RPC/MDT/RPC packages in the middle layer the term superstations is used.

6.7.1 Principle of operation

The RPC is a gaseous parallel electrode-plate (i.e. no wire) detector. Two resistive plates, made of phenolic-melaminic plastic laminate, are kept parallel to each other at a distance of 2 mm by insulating spacers. The electric field between the plates of about 4.9 kV/mm allows avalanches to form along the ionising tracks towards the anode. The signal is read out via capacitive coupling to metallic strips, which are mounted on the outer faces of the resistive plates. The gas used is a mixture of $C_2H_2F_4$/Iso-C_4H_{10}/SF_6 (94.7/5/0.3) which combines relatively low operating voltage

Table 6.10: RPC parameters and performance.

Parameter	Design value
E-field in gap	4.9 kV/mm
Gas gap	2 mm
Gas mixture	$C_2H_2F_4$/Iso-C_4H_{10}/SF_6 (94.7/5/0.3)
Readout pitch of η and ϕ-strips	23–35 mm
Detection efficiency per layer	$\geq$98.5%
Efficiency including spacers and frames	$\geq$97%
Intrinsic time jitter	$\leq$1.5 ns
Jitter including strip propagation time	$\leq$10 ns
Local rate capability	$\sim$1 kHz/cm^2
Streamer probability	$\leq$1%

(due to the low SF_6 concentration), non-flammability and low cost, while providing a comfortable plateau for safe avalanche operation. The main parameters and performance of the RPC's are given in table 6.10 and further details on the parameters in [176].

RPC's can be operated both in avalanche and streamer mode. In the high background environment encountered at the LHC, the avalanche mode offers the benefit of higher rate capability and rate-independent time resolution and has therefore been selected as the operation mode. At the nominal operating voltage of 9.8 kV, a signal with a width of about 5 ns is generated by the track with a streamer probability of less than 1%.

The small jitter of the RPC signal in avalanche mode with respect to the passage of the particle is due to the primary electrons not having to drift to a region of amplification, as is the case in all types of wire chambers. In the strong and uniform electric field inside a RPC cell, all primary electron clusters form avalanches simultaneously, producing *one* single signal instantaneously after the passage of the particle. The charge multiplication in each avalanche continues until its arrival at the anode plane and, therefore, the gas gain of each avalanche depends on the distance of the primary cluster from the anode. The total signal charge is thus dominated by the few clusters produced at the largest distances from the anode. The RPC operating parameters are discussed in [205–207].

6.7.2 Mechanical structure

A RPC trigger chamber is made of two rectangular detectors, contiguous to each other, called units. Each unit consists of two independent detector layers, called gas volumes, which are each read out by two orthogonal sets of pick-up strips.

The structure of the gas volumes (i.e. 1/2 unit) is identical for all RPC's (figure 6.29): two resistive plates (plastic laminate, 2 mm) with a volume resistivity of 10^{10} Ωcm, delimit a gas gap of 2 mm, the correct distance being assured by a series of insulating spacers. The outside surface of the resistive plates is coated with a thin layer of graphite paint (100 k$\Omega/\Box$) to assure the HV and ground connection of the resistive electrodes. The graphite electrodes are insulated from the

2008 JINST 3 S08003

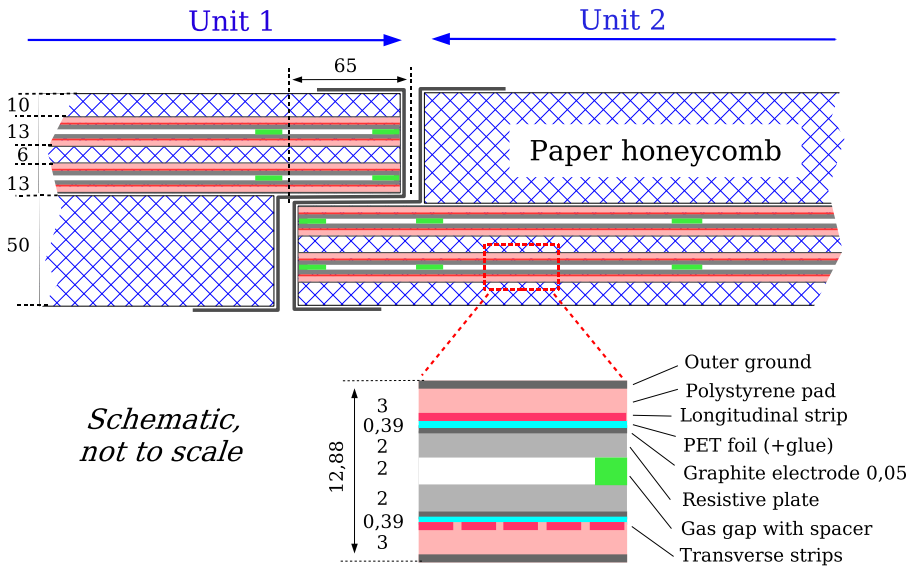

Figure 6.29: Cross-section through a RPC, where two units are joined to form a chamber. Each unit has two gas volumes supported by spacers (the distance between successive spacers is 100 mm), four resistive electrodes and four readout planes, reading the transverse and longitudinal direction. The sandwich structure (hashed) is made of paper honeycomb. The ϕ-strips (measuring the ϕ coordinate) are in the plane of the figure and the η-strips are perpendicular to it. Dimensions are given in mm.

pick-up strips by means of PET films (190 μm), glued to the graphite surfaces. The pick-up strips outside the PET layers are bonded on polystyrene plates (3 mm) and connected to the front-end electronics. The outside surface of the polystyrene plates carries a copper sheet for grounding. A readout signal is induced on the strips by the drift motion of the avalanche electrons. The graphite electrode interposed between the gas gap and the strips does not shield the induction in a significant way due to the graphite electrode's high resistivity and the fast rise-time of the signal.

Each RPC unit is thus made of two detector layers (i.e. gas volumes) and four readout strip panels. The detector layers are interleaved with three support panels made of light-weight paper honeycomb (40 kg/m^3) and are held in position by a solid frame of aluminium profiles. The two external support panels interconnected by the aluminium profiles give the required stiffness to the chamber. The BOL chambers being the largest size ones have a reinforced structure using aluminium plates (2 mm) and aluminium honeycomb. The total thickness of a RPC unit with two gas volumes, support panels and aluminium covers is 96 mm (106 mm for the BOL) and increases to 112 mm (122 mm for the BOL) if the lateral profiles are included. The two units forming a chamber have an overlap region of 65 mm to avoid dead areas for curved tracks. The BMS gas volumes have no physical segmentation in the transverse (ϕ) direction, and thus cover the chamber over its full length. All other standard chambers, whose size exceeds the maximum length (3200 mm) of the available plastic laminates have gas volumes divided in two segments along the ϕ direction with a 9 + 9 mm inefficient region in between due to the edge frames. The readout-strip panels are also segmented in the longitudinal (ϕ) direction, including the case of the BMS, in order to get

an homogeneous trigger scheme for all chamber types. This reduces the η-strips time jitter by a factor of two. RPC's have been certified for high rate operation and ageing at the GIF facility at CERN [208, 209].

All standard RPC's, as listed in table 6.9, are assembled together with a MDT of equal dimensions in a common mechanical support structure. In order to avoid constraining forces amongst the two chamber types, light-weight kinematical supports were used, holding the chambers with minimum clearance as required by the confined radial space.

A number of small RPC chambers (special RPC's) not paired with MDT's are used around the magnet ribs and in the feet region, where MDT's cannot be installed because of lack of space. RPC's, requiring less space, are used in these regions to keep the trigger acceptance loss to a minimum.

6.7.3 Signal path and readout electronics

A RPC operating in the avalanche mode produces signals of 5 ns full width at half-maximum with a time jitter of 1.5 ns. To preserve this high inherent precision, the pick-up strips must be high-quality transmission lines with low attenuation, terminated at both ends with the characteristic impedance.

The layout of a readout strip plane is shown in figure 6.30. The strips with a width of 25–35 mm consist of 17 μm copper on a 190 μm PET foil glued on a 3 mm plate of rigid polystyrene, which is covered, on the outside, by 50 μm PET and 17 μm copper as ground reference. The strips are separated by a 2 mm gap with a 0.3 mm ground strip at the centre for improved decoupling. This sandwich structure creates an impedance of about 25 Ω for the strips, slightly depending on the width.

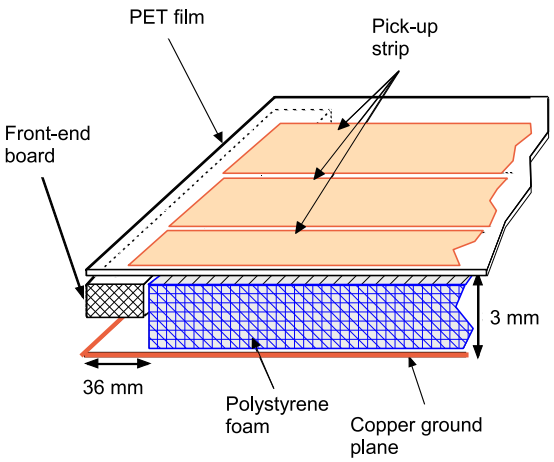

Figure 6.30: Layout of a RPC readout strip plane.

The front-end circuit is a three-stage shaping amplifier followed by a comparator. It is implemented in a eight-channel GaAs die (in order to avoid the encapsulation cost) which is bonded with 20μm-diameter gold wire on a printed board serving eight strips. The boards are mounted along the edges of the readout panels as shown in figure 6.30 and soldered directly to the strips thus avoiding the introduction any further insensitive area in addition to those already contained in the gas volume. While this prevents exchange of faulty amplifiers in the field, the known reliability of GaAs-ASIC's minimises the risk of losing readout channels during the experiment.

The frequency response of the GaAs-amplifiers has a maximum at 100 MHz and a 60 MHz bandwidth, well adapted to the rise time of the chamber signals. The front-end electronics input is coupled to the strips with a transformer integrated in the printed circuit matched to the signal polarities of η and ϕ-strips, which are opposite to each other. The voltages defining the thresholds

Table 6.11: Location and radial extension of the TGC wheels. All dimensions are in mm.

	EM big wheel			**I layer**	
	M1 triplet	M2 doublet	M3 doublet	FI (small wheel) doublet	EI doublet
Overall centre in z	13440	14733	15153	6983	7370
Inner radial extent	1900	2526	2610	2170	4700
Outer radial extent	10682	11917	11917	4434	6190

of the comparators are supplied by external digital-to-analogue converter units, located in racks in the experimental hall controlled via the DCS. Details of the RPC front-end electronics are given in [210, 211].

The front-end output signals of the ϕ-strips are wired OR-ed such that two physical strips form a logical strip of twice the length but with the same time jitter as a single strip. This is done to avoid unnecessary granularity and to adapt the RPC readout segmentation to the trigger sector segmentation as discussed in section 8.2.2. The ϕ-strip length and the relative time jitter is on average about half that of an η-strip, giving the ϕ-strips a more precise timing.

In order to be used for the trigger, a signal from a RPC has to be compared with those in the two other RPC's along the path of the particle, i.e. in the same sector and tower, a task which is accomplished by a system of fast coincidence units close to the chambers. Thus, coincidences between strips in RPC1 and RPC2 are used to create the low-p_T trigger. A high-p_T trigger requires hits in all three trigger stations: RPC1 and RPC2 must fulfil the low-p_T condition *and* a confirming hit must be found in RPC3. The inclusion of the low-p_T trigger condition in the high-p_T trigger definition leads to more robustness against fake triggers compared to a simple coincidence between RPC3 and only one inner RPC station. A detailed discussion of the RPC trigger system is given in section 8.2.2.1.

6.8 Thin gap chambers

6.8.1 Introduction

Thin Gap Chambers (TGC's) provide two functions in the end-cap muon spectrometer: the muon trigger capability and the determination of the second, azimuthal coordinate to complement the measurement of the MDT's in the bending (radial) direction. The middle layer of the MDT's in the end-cap (EM-wheel) is complemented by seven layers of TGC's, while the inner (I) layer is complemented by only two layers. The inner layer is segmented radially into two non-overlapping regions: end-cap (EI) and forward (FI, also known as the small wheel). EI TGC's are mounted on support structures of the barrel toroid coils.

The azimuthal coordinate in the outer MDT wheel (EO), i.e. the coordinate along the tube, is obtained by the extrapolation of the track from the middle layer, which can be done accurately due to the lack of magnetic field between EM and EO.

The radial, bending coordinate is measured by the TGC wire groups, the azimuthal coordinate by the radial strips. The TGC's need good time resolution to tag the beam-crossing with high efficiency ($\geq 99\%$) and fine granularity to provide a sufficiently sharp cut-off in the momentum of the triggering muon. To match the granularity to the required momentum resolution, the size of the wire groups varies from 6 to 31 as a function of η, corresponding to a variation in width from 10.8 mm to 55.8 mm. The alignment of wire groups in consecutive layers is staggered to optimise the position resolution for a given number of electronics channels. The radial strips are staggered in a similar way to achieve an azimuthal granularity of 2–3 mrad, as seen from the interaction point.

Figure 8.9 shows a longitudinal cut through the end-cap. TGC's are located in the innermost layer (marked I) and in the middle layers (EM-wheels marked M1–M3, corresponding to TGC1–3). The location of the MDT in a small (S) and large sector (L) are shown for reference. The location along z and the radial extension of the TGC wheels are given in table 6.11. A detailed listing of all relevant construction parameters is given in the TGC parameter book [212].

6.8.2 Principle of operation

The main operational parameters of the TGC's are summarised in table 6.12.

TGC's are multi-wire proportional chambers with the characteristic that the wire-to-cathode distance of 1.4 mm is smaller than the wire-to-wire distance of 1.8 mm, as shown in figure 6.31. With a highly quenching gas mixture of CO_2 and n-C_5H_{12} (n-pentane), this cell geometry allows for operation in a quasi-saturated mode, i.e. with a gas gain of $\sim 3\times10^5$. This relatively low gas gain, compared to previous implementations of the TGC concept, does not allow to make full use of its independence from the primary ionisation. Some of its characteristics are still kept, even at such a low gas gain. In particular:

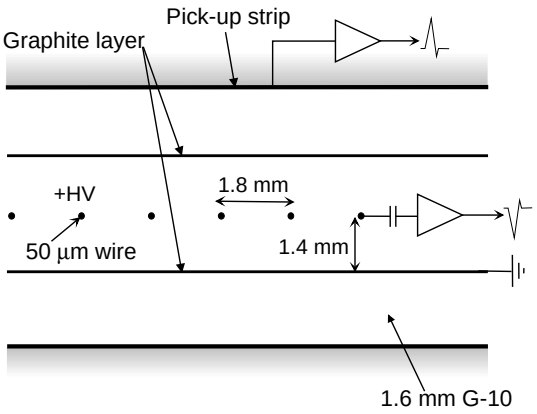

Figure 6.31: TGC structure showing anode wires, graphite cathodes, G-10 layers and a pick-up strip, orthogonal to the wires.

- The highly quenching gas prevents the occurrence of streamers in all operating conditions.
- The pulse height observed in the interaction of low energy neutrons (1–10 MeV) is only a factor 30 larger than for a minimum ionising particle.

The high electric field around the TGC wires and the small wire-to-wire distance lead to very good time resolution for the large majority of the tracks. Only tracks at normal incidence passing midway between two wires have much longer drift times due to the vanishing drift field in this region. This effect was already discussed in the context of the CSC's which have a similar cell geometry, see section 6.4.2. In the TGC wheels, however, the angle of incidence for tracks emerging from the

Table 6.12: Main TGC operational parameters.

Parameter	Design value
Gas gap	2.8 ± 0.10 mm
Wire pitch	1.8 ± 0.05 mm
Wire diameter	50 μm
Wire potential	2900 ± 100 V
Operating plateau	200 V
Gas mixture	CO_2/n-pentane (55/45)
Gas amplification	3×10^5

interaction point will always be greater than 10°, thus a part of the track will be outside of the low field region. Including the variation of the propagation time on wires and strips, signals arrive with 99% probability inside a time window of 25 ns.

6.8.3 Mechanical structure

The seven detector layers in the middle layers (big wheels, see section 9.5) are arranged in one triplet and two doublets. The triplet is to cope with false coincidences from background hits, which are more likely in the end-cap region than in the barrel.

The trigger detectors, forming circular disks, are mounted in two concentric rings, an outer or end-cap one covering the rapidity range $1.05 \leq |\eta| \leq 1.92$ and an inner or forward one covering the rapidity range $1.92 \leq |\eta| \leq 2.4$. Figure 6.32 shows the cross-section of a TGC triplet and doublet. The structure consists of wire planes (anode), cathode planes, strip planes, shields and honeycomb support structures. The cathode planes consist of 1.6 mm thick FR4 (Flame Resistant 4) plates, graphite coated on the inside, i.e. facing the wires, and with copper cladding on the other side. The resistivity of the graphite is of 1 M$\Omega/\Box$ in the end-cap and of 0.5 M$\Omega/\Box$ in the inner/forward region. Two of the copper layers in the triplet and doublets are segmented into readout strips to read the azimuthal coordinate (marked "Cu strips" in figure 6.32). The solid copper layers serve as DC grounds, while the segmented ones, being connected to amplifiers, are virtual grounds for the wire signals. On the outside of the triplet and doublet chambers the honeycomb stiffeners are covered by 0.5 mm thick FR4 plates for rigidity and mechanical protection. The adjacent chambers in a module (three in a triplet, two in a doublet) are separated by a 20 mm thick honeycomb paper stiffener.

A gas volume containing a wire plane and two cathodes is called a chamber, while the entirety of three or two chambers in a triplet or doublet arrangement is called a unit. In the outer ring four or five chambers in triplet and doublets, respectively, are mounted in the way of a ladder forming modules. All TGC's in the big wheel (EM) are segmented into 12 sectors of 30° in the azimuthal direction. Thus, a sector in the outer ring comprises four modules of 7.5°, while the inner ring has two modules of 15°. Altogether there are 744 units in the big wheels, corresponding to 1704 chambers. The TGC wheel in the innermost layer has a slightly different geometrical structure, containing 45 units and 90 chambers on each side. A summary of the TGC segmentation is given in table 6.13.

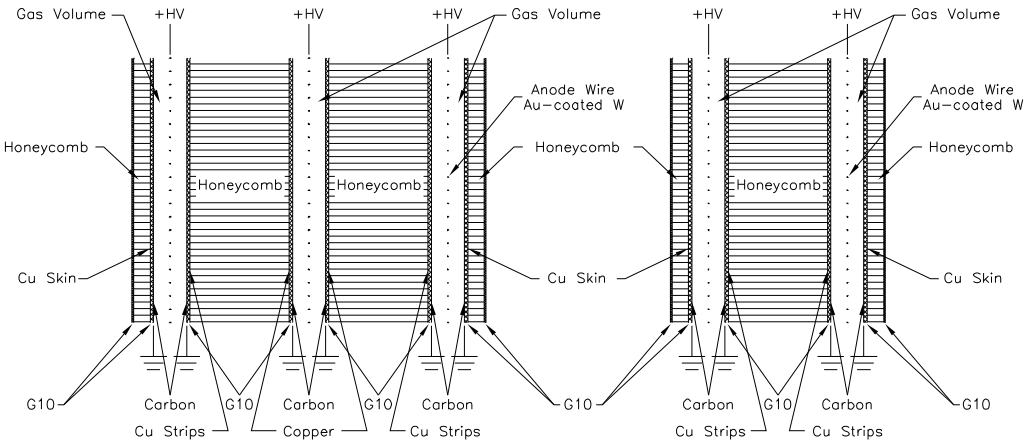

Figure 6.32: Cross-section of a TGC triplet and doublet module. The triplet has three wire layers but only two strip layers. The dimensions of the gas gaps are enlarged with respect to the other elements.

Table 6.13: TGC modularity. Each wheel consists of 12 sectors, each sector containing an inner (forward) and an outer (end-cap) part, having a different azimuthal segmentation. A module covers 15° in azimuth in the inner and 7.5° in the outer part.

	EM big wheel						**I layer**		**Total**
	M1 triplet		M2 doublet		M3 doublet		I doublet		
Modularity	Inner	Outer	Inner	Outer	Inner	Outer	Inner	Outer	
Modules/sector	2	4	2	4	2	4			
Units/module	1	4	1	5	1	5			
Chambers/unit	3	3	2	2	2	2			
Units/sector	2	16	2	20	2	20			
Units/side	24	192	24	240	24	240	24	21	789
Units/system	48	384	48	480	48	480	48	42	1578
Chambers/sector	6	48	4	40	4	40			
Chambers/side	72	576	48	480	48	480	48	42	1794
Chambers/system	144	1152	96	960	96	960	96	84	3588

All TGC units are enclosed on their periphery by a gas-tight envelope which is continuously flushed by CO_2. This is done to keep a dry atmosphere in the region where the HV elements are located as well as to dilute any potential leak of the operating gas (n-pentane). If traces of this flammable gas are detected in the CO_2 stream at the output of the chambers, HV and LV as well as gas supplies are automatically switched off, and an alarm is activated.

6.8.4 Signal path, readout, and detector controls

The data flow starting with the primary wire and strip signals is as follows. After amplification in the front-end amplifiers, signals are time-aligned and synchronised to the beam-crossing frequency. The subsequent signal processing makes use of the redundancy of the track measurement in the

TGC layers to mitigate the effects of chamber inefficiencies and improve rejection of fake triggers caused by background or noise hits. Thus the three signals of the triplet are combined to form a 2-out-of-3 coincidence, while the four signals of the two EM-doublets form a 3-out-of-4 coincidence. Track segments which have passed this early filter are forwarded to the coincidence matrix, which performs a fast search for signal coincidences corresponding to muon tracks in a certain momentum range. A detailed description of the algorithm used and of the signal processing in the higher levels of the trigger system is given in chapter 8.

The detector control system (DCS) is fully integrated into the trigger electronics. For the TGC, its role is not only of monitoring operating parameters like temperatures, voltages and currents as well as the relative alignment of the detectors (down to 0.2 mm), but it can also initialise its various elements. Furthermore, by combination with a special trigger signal of the patch-panel board, it can monitor the charge left by an ionising particle in every chamber, and therefore act as a gas monitor for every single detector.

6.9 Commonalities in the muon system

6.9.1 The gas supplies in the muon system

While gas mixtures and operating conditions in the sub-systems of the muon spectrometer are quite different, being adapted to the requirements of the four chamber types, there are also many commonalities amongst them from an operational point of view.

- The gases must be circulated in a closed loop system (mainly for cost reasons), except for the CSC's. This requires a complex recuperation and re-mixing system, using specialised purifiers to clean the gas before recirculation into the supply system. For safety and space reasons, all recuperation systems are housed on the surface, requiring tight pressure and flow control for the transfer to the underground experimental area.

- Distribution of the gas in the experimental cavern needs a high degree of modularity to be immuned to leaks in any given supply line. Because of the considerable hydrostatic pressure variations along the height of the hall (25 m), pressure regulation has to be segmented accordingly. Therefore, gas distributors (racks) are located at three different levels in the galleries and wheels of the detector each one supplying chambers in a ± 3 m range of relative elevation.

- The flow rate in the gas distribution branches must be supervised by a correspondingly large number of flow and pressure meters for control of gas circulation (purity), operating pressure and leak detection. Precise pressure control is most important for CSC, RPC and TGC chambers, where operation is defined at ~ 2 mb above the outside pressure at the corresponding height and where a significant overpressure might lead to the destruction of the chamber. While this is not the case for the MDT's, they also need precise pressure control for reasons of drift time and gain stability.

Besides these commonalities there are many differences due to the particularities of the gases used in each system. The high flammability of the TGC gas mixture, for example, requires stringent

Table 6.14: Main characteristics of the muon gas supply systems.

Characteristic	MDT	CSC	RPC	TGC
Gas mixture	$Ar/CO_2/H_2O$	Ar/CO_2	$C_2H_2F_4$/Iso-C_4H_{10}/SF_6	CO_2/n-pentane
Composition	93/7/($\leq$ 1000 ppm)	80/20	94.7/5/0.3	55/45
Gas gain	2×10^4	6×10^4	10^7	3×10^5
Flammability	—	—	low	high
Operating pressure (bar)	3	1	1	1
Volume at operating pressure (m^3)	710	0.5	14	16
Gas exchanges/day	1	10	20	4
Flow at operating pressure (m^3/h)	30	0.2	12	2.7

safety precautions, the outside of the TGC's being constantly flushed with CO_2 in a separate, closed gas circuit. The return gas is monitored for traces on n-pentane, which could point to leaks in the primary distribution system.

The main characteristics of the four gas supply systems are summarised in table 6.14 and in more detail in table 9.5.

6.9.2 Electronics services and power consumption

The segmentation of the electrical services of the muon system follows the structure of the detector which is characterised by a high level of modularity, consisting of electrically independent chambers. The service architecture aims to match this modularity in order to limit data loss in case a given supply channel should fail. Power supply channels are kept floating i.e. the ground outputs of the power supplies are not connected amongst each other nor to the power supply housing or to any local safety ground. This way, the return current of a given chamber has only one path to return to its power supply. Ground loops (multiple ground returns) are therefore not possible. Ground loops, if present, might create noise coupling between near-by chambers and would expose the readout to noise pick-up from sources in the ATLAS electrical environment. To further prevent pick-up, all low-voltage (LV) supply cables are shielded by a copper mesh enclosing the cable wires. The cable shield is connected only at one end (chamber side) to the return wire.

For the definition of the DC level and for safety reasons all chambers are connected from one point of the chamber to the ATLAS structure ground. This star grounding does not allow currents to circulate, i.e. does not create ground loops.

For cost reasons, the maximum supply modularity could not be maintained. Thus, every two MDT chambers are supplied from one LV supply channel. The segmentation of the MDT high-voltage (HV) supplies is finer, with each multi-layer of three (four) tube layers being supplied by a separate channel. Close to the chamber, a passive HV-split is installed (splitter box) to supply each tube layer with an independent cable. In case of shorted tubes (broken wire), the corresponding tube layer can be disconnected, while the other layers would continue to work. Under normal LHC conditions and at an operating voltage of 3080 V, typical chamber currents are around 100 μA, yielding a negligible heat dissipation of about 0.3 W/chamber. The total LV power consumption of the MDT system is about 38.5 kW. Only one 4.5 V supply line is needed for each MDT chamber with an average consumption of about 25 W.

The CSC LV system supplies one voltage of 9 V. The operating voltages of 3.3 V and 5 V are derived with radiation tolerant regulators close to the chamber. Each of the 16 chambers of an end-cap consumes about 40 A, leading to a total consumption of about 11.5 kW for both end-caps. The power dissipated in the readout electronics, is evacuated by a water cooling system. The RPC's have separate LV supplies for the analogue front-end and the digital (trigger) electronics, operating at -5 V and 3.3 V, respectively. A third voltage of -2 V is needed to supply the wired-ORs (pull down voltage), combining two aligned physical wires into a "logical" wire. A number of reference voltages are supplied to each chamber to define the discriminator thresholds for the ASD boards. The total power consumption of the RPC system is about 42 kW. The HV for the RPC's (9.8 kV) requires one channel for each gas gap. To limit the required number of primary supply channels, splitter boxes are used, which are able to safely handle voltages up to 15 kV.

All power supply channels for the MDT barrel, the CSC's, RPC's and TGC's in the small (EI) wheel are housed in racks in the UX15 experimental hall and have been certified for tolerance to radiation and magnetic field. The TGC chambers and the MDT in the big wheel (EM wheel) are supplied from racks directly mounted on the wheel structure (non-standard "mini-racks", due to space limitations at the circumference of the EM wheel) in order to limit cable lengths and power loss on the LV cables.

The TGC's, like the RPC's, have separate LV supplies for analogue and digital readout electronics. The segmentation of the supplies in the EM wheel follows that of the TGC's, with 12 sectors per side. For the small wheel there is only one supply channel per side for each voltage. The HV modularity provides one supply channel per chamber with the exception of the 144 inner chambers in the M1 triplet which have two supply channels per chamber. A total of 3732 HV channels are therefore used to serve the 3588 chambers of the TGC system.

Services for the small wheel, containing MDT's, CSC's and TGC's, are routed through a flexible support structure (cable chains). When the small wheel is moved along the z-direction to give access to the calorimeters and inner detector, most service channels will not require interruption, reducing access time and minimising the risk of damage to the small wheel chamber operation.

An overview of the segmentation and power consumption of the four muon sub-systems is given in table 6.15.

Table 6.15: Power consumption of the four sub-systems of the muon spectrometer. Voltages delivered by the power supplies (column 2) are approximate, depending on cable length and conductor cross-section. The differences between power *supplied* and *consumed* are due to cable losses as well as losses in voltage regulators, used to stabilise voltages on the board. The aim of the cabling layout was to limit cable losses to about 15–20% of the power used by the circuits. This could not be achieved for the CSC's due to limitations on cross-sections for supply cables. The PS-boards and HS-crates are components of the TGC digital readout (see section 8.2.2).

	Voltage at power supply	**Voltage on circuit**	**Supply channels**	**Average current per channel**	**Average power per channel**	**Total power (both sides)**	
						consumed	**supplied**
	V	V	Number	A	W	kW	kW
MDT							
- mezzanine cards & CSM	4.5	3.3	1140	7.5	25	28.2	38.5
CSC (ASM-I & ASM-II)							
- analogue front-end	9	3.3	32	5	17	0.5	1.4
- digital read-out	9	5	32	35	175	5.6	10.1
RPC							
- analogue front-end	-6.7	-5	528	4	20	10.6	14.2
- wired-OR (pull-down)	-2.3	-2	408	0.2	0.4	0.2	0.2
- splitters & PAD boards	4.3	3.3	400	16	53	21.1	27.5
TGC EM wheel							
- analogue front-end	3.3	3	24	217	651	15.6	17.2
- analogue front-end	-3.3	-3	24	56	168	4.0	4.4
- readout (PS-boards)	3.4	3.3	24	55	182	4.4	4.5
- readout (HS-crates)	3.3	3.3	24	34	112	2.7	2.7
TGC EI wheel							
- analogue front-end	3.5	3	2	80	240	0.5	0.6
- analogue front-end	-3.5	-3	2	18	54	0.1	0.1
- readout (PS-boards)	3.3	3.3	2	25	83	0.2	0.2
Total power muon spectrometer						94	122

2008 JINST 3 S08003